Robotic Exoskeletons for Torso Study, Training, and Assistance

Rosemarie Murray

Submitted in partial fulfillment of the
requirements for the degree of
Doctor of Philosophy
under the Executive Committee
of the Graduate School of Arts and Sciences

COLUMBIA UNIVERSITY

2022

Abstract

Robotic exoskeletons are important tools in medicine for characterizing certain aspects of diseases, enabling physical therapy treatments, or providing assistance to those with impairments. One area in particular where these devices can make an impact is the study and treatment of scoliosis. First, I adapt a design of a robotic torso exoskeleton to serve the population most susceptible to scoliosis, female adolescents. I used the device to compare the torso stiffness of members this group with and without scoliosis, and found an interaction effect of degree of freedom (DOF) and torso segment on translational stiffness, and an interaction effect of DOF and group on rotational stiffness. These results can inform the models used to create rigid orthoses for conservative treatment or to simulate the effects of surgical procedures. Second, I explore the effects of different types of augmented sensory feedback commonly used in scoliosis physical therapy. I compare visual and force feedback provided by the exoskeleton on one's ability to replicate static poses and dynamic movements. I find that while force feedback leads to faster initial improvement, visual feedback may enable the user to learn finer details of the movement. Third, I design a torso exoskeleton for people with neuromotor impairments. People who are not able to sit up independently are at a high risk of developing neuromuscular scoliosis, and must balance the benefits of treatment with rigid orthoses, with the limits that these devices place on functional movements. The device allows users four degrees of freedom, to support functional movements such as reaching and pressure relief maneuvers, but prevents lateral translation and axial rotation, which can contribute to neuromuscular scoliosis. Together, these results demonstrate the potential for robotic exoskeletons in torso study, training, and assistance.

Table of Contents

List of Figures

List of Tables

Acknowledgements

I would like to thank my advisor, Dr. Sunil Agrawal for his guidance, and my committee members, Drs. Kristin Myers, Matei Ciocarlie, Andrew Gordon, and Victoria Lent, for their time and feedback on my dissertation. I would like to thank my research mentors, Joon Hyuk-Park and Paul Stegall,for laying the foundation of this work and for inspiring me to pursue my Phd. I would also like to thank Rebekah Wallach, Aruna Chavali, Erika Chan, Isabella Leone, and the students of Marymount school for their assistance with data collection and recruitment. I would like to especially thank Chawin Ophaswongse, my labmate and partner in much of this research. Finally, I owe a great deal of thanks to all of my labmates in the Roar lab for their help, friendship and encouragement throughout the Phd process.

Introduction

The torso and spine are a fundamental to a variety of human movements. Robotic exoskeletons have been used in a variety of situations to assist with physical therapy or with completing everyday tasks. However, most of these devices focus on the limbs. The torso, though it is foundational to motor development, is often overlooked. Yet dysfunction in the spine and torso can cause significant pain and impairment.

One common type of dysfunction is scoliosis, which is an abnormal curvature of the spine out of the sagittal plane. It can cause joint and muscle pain as well as dissatisfaction with body image. At more severe levels, it can put pressure on nerves, or even impinge on the heart and lungs. Scoliosis can develop due to congenital malformations of the vertebrae (congenital scoliosis), as a consequence of a neuromuscular impairment (neuromuscular scoliosis), or due to no known cause (idiopathic scoliosis). For about 90% of children with idiopathic scoliosis, it develops between the ages of 11-18, when the spine is growing rapidly [1]. This type, known as adolescent idiopathic scoliosis (AIS), has a prevalence of 4.7-5.2% [1]. Without treatment during this crucial time period, the spine can curve to more than 50°. If it progresses to that point, the spine will often continue to curve more and more in adulthood unless the patient undergoes a spinal fusion surgery [2]. This procedure is extremely invasive, has a long recovery and a high potential for complications, and also permanently restricts one's range of motion. Fortunately, this outcome can usually be avoided through appropriate conservative treatment. The gold standard for conservative scoliosis treatment is intensive bracing with a rigid thoracolumbar orthosis. Bracing for over 16 hours per day until skeletal maturity can alter the natural history of scoliosis

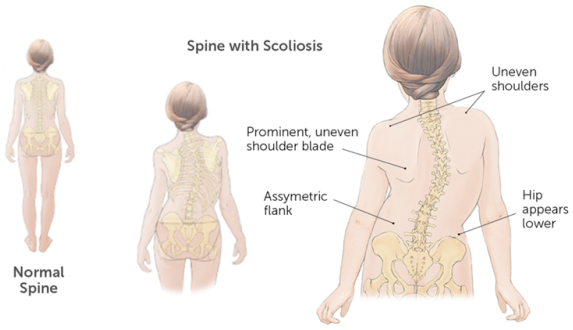

Figure 1: Illustration of adolescent idiopathic scoliosis. [3]

progression and reduce the likelihood of needing surgery [2].

However, despite a general consensus on the effectiveness of bracing, outcomes vary widely between individuals.

Traditionally, braces are made through conventional casting methods and their results often depend highly on the skill of the orthotist. Recently, some researchers have developed finite element models (FEM) or multi-body models (MBM) of the spine-torso system that promise to simulate the effects of bracing [4]. Techniques have been developed to personalize these models based on traction or lateral bending radiographs [5] or computed tomography [6]. FEM has been used in conjunction with CAD/CAM to create rigid TLSO's that provide greater in-brace correction with less surface covering and thinner material [7]. One limitation of these models, however, is that they are based on either the material properties of the in vitro spine available in literature, or on radiographs under different loading conditions. The former may not match the characteristics of population in need of scoliosis treatment, since the specimens obtained were generally from elderly individuals and those undergoing scoliosis treatment are likely to be adolescents. The latter approach is limited in how much data can be provided because of the radiation risk, and might not be able to create a detailed characterisation. Perhaps due to these limitations, FEM approaches to brace construction have not been shown to result in improved clinical outcomes [8].

Some work has been done on the creation of flexible bracing systems, which promise improved patient compliance resulting from improved comfort and quality of life over traditional rigid

braces [9, 10, 11, 12]. These devices aim to control the forces applied to the spine, rather than restricting its position. For this application, a detailed understanding of the stiffness characteristics of the torso is even more important, because the force on the torso must be calculated not just for one position, but for a localized area around the target position. Some evidence suggests that they may be effective for milder scoliotic curves, but less so with moderate to severe curvature [9]. Greater understanding of the stiffness characteristics of the torso may improve the design of these devices.

Prior work has evaluated the stiffness of the torso in rotation, but has failed to fully characterize the three-dimensional nature of the torso stiffness [13]. A full characterization of the coupling between forces and displacements is needed because scoliosis treatment involves precise repositioning of the torso in multiple degrees-of-freedom at the same time. A moment applied about a particular axis may result not only in rotation about that axis, but also rotations about other axes and translation in three-dimensional space. To capture this complex relationship between force and displacement in the torso, one needs to calculate the 6×6 stiffness matrix of the torso. In addition, previous work has focused on the torso as a whole rather than separately articulating the lumbar and thoracic regions. However, with the development of the Robotic Spine Exoskeleton (RoSE), our group has previously presented a three dimensional stiffness of adult male torsos without spinal deformity, as well as a case study of an individual with kyphosis and an individual with scoliosis [14].

Most cases of scoliosis develop during adolescence, and while there is strong evidence to support bracing treatment during adolescence, there is little compelling evidence that bracing in adults can improve curvature or prevent further progression [15]. Consequently, information about adolescent torso stiffness is more relevant to the current treatment that information about adults. In addition, scoliosis affects females more than males, and the ratio increases with the severity of the curve. Therefore, female adolescents are most at risk to develop curves that require surgical intervention.

Therefore, in chapter 1, we present the design of the robotic spine exoskeleton adapted to the

Figure 2: Robotic Spine Exoskeleton designed for female adolescents

needs of the clinical AIS population. In chapter 2, we use this device to create a first characterization of the three-dimensional stiffness of the in vivo torso in adolescent females with and without scoliosis. This study provides insight into the similarities and differences from a biomechanical perspective of adolescents developing typically versus those developing an abnormal spinal curvature. It also provides data that could help orthotists produce more effective torso orthoses for conservative scoliosis treatment.

Another important tool in conservative scoliosis treatment is physical therapy. Scoliosis-specific therapy helps patients learn how to achieve alignment with their own muscle effort. It can help reduce pain in the brace, improve balance, and prevent muscle atrophy during bracing [16, 17]. It has been shown to reduce curve progression when used in complement with rigid bracing, and to stabilize curve progression when weaning off the brace [18]. However, it is a difficult task because self-correcting one's spinal alignment requires conscious, point-by-point control of the spine, rather than the unconscious, general control that one usually applies to the spine. Research also suggests that AIS may be associated with impaired sensory integration of the visual, vestibular, and proprioceptive senses [19, 20, 21, 22, 23], and that those with scoliosis have an impaired ability to control specific segments of the spine [24]. Even their subjective sense of

Figure 3: Physical therapy for scoliosis

vertical may be affected [25].

Most schools of scoliosis-specific physical therapy employ augmented sensory feedback to help patients develop a better sense of their postural alignment and to fine tune the motor control of their trunk [**Smania2009**]. The sensory feedback tools are usually visual or somatosensory cues. For example, the clinician might use a mirror to point out how the patient's alignment could be improved, or placing their hand against the area of the curve the patient should try to move [26]. Once the patient can achieve the desired posture with the help of this sensory feedback, the feedback is slowly weaned away, with the goal that the patient is able to assume the posture consciously, through only their proprioceptive sense, and then eventually that they are able to integrate it into their unconscious postural control. However these augmented feedback strategies are limited. Mirrors can only show certain angles of the body, and can only show the patient their current position, not how their body would look in a healthy posture. As far as somatosensory cues, clinicians can touch or apply pressure to different areas of the torso, but are limited in how precise they can be.

Robotic exoskeletons have proven to be valuable tools for rehabilitation in populations with

neuromotor impairment, such as stroke, spinal cord injury, and cerebral palsy [27]. These interventions give clinicians the ability to provide their patients with augmented sensory feedback in a precise and repeatable way. For example, an exoskeleton with assist-as-needed controller could provide somatosensory feedback by guiding a patient to move through a specific joint trajectory. Alternatively, it could provide visual feedback to the user about where their limb is in regard to the desired movement. These devices have shown marked contributions in gait training [28] and upper-limb rehabilitation [29].

However, the trunk-training rehabilitation robots that have been developed have focused on improving seated or standing balance [30, 31], or enhancing reaching ability [32]. These are important tasks, but they aim to enhance the unconscious, indirect postural control strategy that most people already use in their day to day, rather than providing the augmented sensory feedback required to develop the conscious, direct postural control needed in scoliosis physical therapy. On the other hand, the Robotic Spine Exoskeleton (RoSE), has a high degree of specificity, with six degrees of freedom at both the lumbar and thoracic level. It also has the capacity to apply forces and moments to the user, and to detect (and display visually) their position. These features enable us to provide augmented sensory feedback to the user, to help them learn a novel posture or spinal motion. In chapter 3, we present the first application of a robotic torso exoskeleton for augmented sensory augmentation in direct trunk posture learning.

While the previous studies looked at ways in which conservative treatment for AIS could be improved, another major population in need of scoliosis research and treatment tools is those with neuromotor impairments in the torso. In this group, scoliosis often develops as a secondary condition. AIS has a prevalence of 0.47-5.2% of the general population, but scoliosis develops in 25% of people with cerebral palsy, 80% of those with Friedrich's ataxia, 90% of those with Duchene's myopathy, and up to 100% of children with spinal cord injuries [34, 35].

These condition can all cause an inability to sit upright independently. If someone cannot sit up by themselves, they might compensate by using their hands for support, or by leaning against a backrest or the side of a chair. However, these strategies make it difficult to perform functional

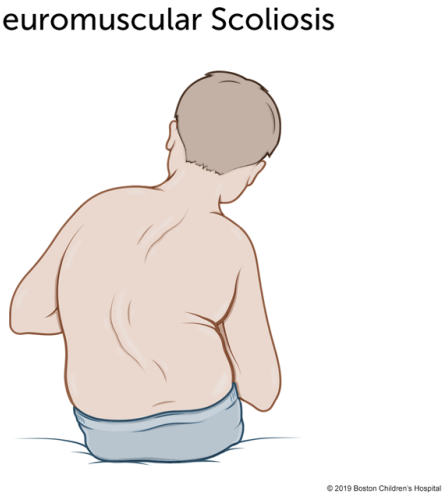

Figure 4: Illustration of neuromuscular scoliosis. [33]

tasks, such as eating a meal, getting something from a shelf, or propelling a wheelchair. Someone with trunk motor impairments may fall while doing these tasks, or may avoid these activities out of fear of falling [36, 37]. In addition, constant leaning can put the spine at risk for scoliosis development, particularly if the spine is still growing. For example, children with cerebral palsy and GMFCS levels of IV and V have a 50% chance of developing moderate or severe scoliosis by age 18, but children with GMFCS levels of I and II (capable of independent sitting) have almost no risk. [38]. Finally, people with greater levels of impairment, such as those with cervical spinal cord injuries, may struggle to shift their center of pressure in the chair. This can put them at risk for pressure sores, which can then trigger autonomic dysreflexia [39]. To counteract these problems, an assistive device capable of supporting users through a range of seated postures is needed.

Current solutions to these problems consist of a variety of passive and generally static devices, such as cushions, straps, thoracolumbosacral orthoses (TLSOs), wheelchair tilt, and caregiver assistance. Cushions help promote good static posture and pressure distribution, but do not provide dynamic assistance and can be difficult to position consistently. Straps can help prevent falling, but also inhibit reaching and performing functional tasks. TLSOs do not affect the natural

history of neuromuscular scoliosis [40], but may make it possible to delay surgery in adolescents. However, they are extremely restrictive and can result in muscle atrophy. Wheelchairs with recline and tilt-in-space features can help distribute pressure [41], but do not allow one to lean forward effectively and cannot easily be incorporated into dynamic movements. Caregivers can also assist someone to shift their posture and center of pressure, but this can put strain on the caregiver and limit patient independence. In recent years, some robotic posture devices have also been developed. A novel mechanism has been proposed [42] to provide posture support to individuals with spinal cord injury. However, this device is passive and does not provide lateral support. Other torso exoskeletons have been proposed [43, 44, 30], but are not suited to the unique needs of this group.

In chapter 4, a novel wheelchair-mounted robot for active postural support is designed to aid individuals with trunk motor control impairments. It supports a user in upright sitting and allows them motion in the sagittal plane as well as lateral bending, which are required for activities such as reaching movements and pressure relief maneuvers. At the same time, it prevents the "windswept" posture associated with neuromuscular scoliosis, by inhibiting pelvic obliquity, and lateral translation and axial rotation of the trunk.

Following this introduction, chapter 1 describes the robotic spine exoskeleton adapted for female adolescents. Chapter 2 presents the torso stiffness characterization for female adolescents with scoliosis as well as healthy controls. Chapter 3 explores the effect of augmented sensory feedback provided by the robotic exoskeleton on direct trunk posture learning. Chapter 4 presents the design of a wheelchair-mounted robot for active postural support that can provide assistance to those with trunk neuromotor impairments and prevent postures associated with neuromuscular scoliosis. The dissertation is concluded with a summary of the contributions and recommendations for further research.

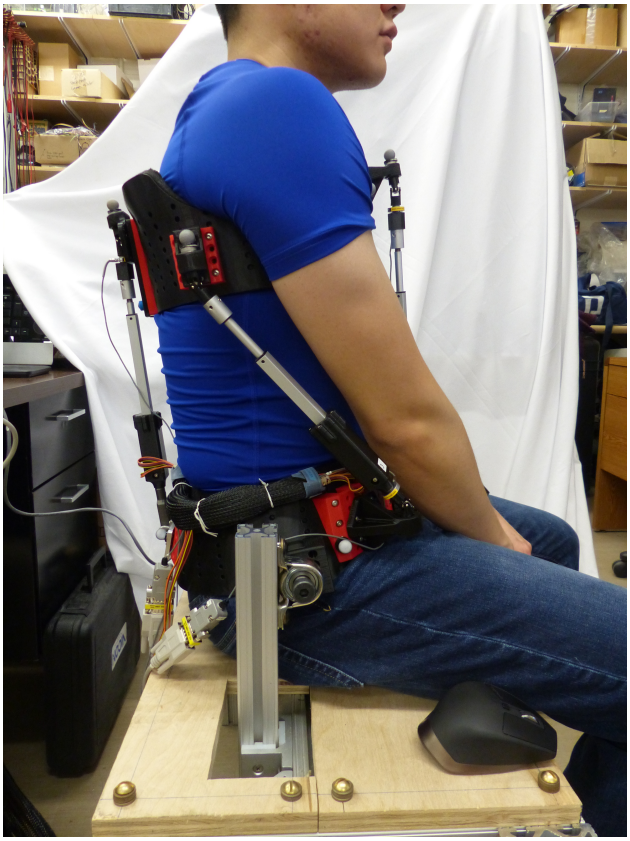

Figure 5: Wheelchair Robot for Active Postural Support, designed for individuals with torso motor impairments.

Chapter 1: Robotic Spine Exoskeleton

The Robotic Spine Exoskeleton (RoSE) developed for this work is adapted from the design presented in [45]. The earlier design provided a proof of concept, but it was built to fit adult men, who are unlikely to require conservative scoliosis treatment. Idiopathic scoliosis most often occurs during adolescence, when the spine is growing rapidly. Adolescent idiopathic scoliosis (AIS) accounts for approximately 90% of idiopathic scoliosis in children with an overall prevalence of 0.47–5.2% [1]. While AIS can affect both male and female adolescents, girls face an increased prevalence particularly at higher levels of severity. The female to male ratio for mild cases is 1.4:1, but increases to 7.2:1 for severe curves (curve angle >40°) [1]. Clearly, in order to study the largest clinical population for scoliosis treatment, the robotic exoskeleton must accommodate adolescent girls.

As shown in Fig. 1.1, the robotic spine exoskeleton consists of three rings around the torso connected in a double Stewart platform design. The rings are cut from an off-the-shelf thoracolumbar orthosis (Original Boston Brace, Boston Orthotics & Prosthetics, MA). The limbs are connected to the rings through attachments designed with CAD (Solidworks,MA) and 3D printed (Fortus 360mc, Stratasys, MN) in ABS. Each of the twelve limbs contains a linear actuator (L12-50-210-12-P, Actuonix, Canada). They have a 5 cm stroke length, a max speed of 6.2 mm/s, and a max force of 80 N. They are driven with TB6612FNG dual motor driver (Toshiba, CA). The onboard potentiometers' signals are multiplexed and sent to the control board (myRio-1900, National Instruments, TX). The motors are placed in series with load cells (LCM200, Futek, CA). The signals from these load cells are amplified (CSG110, Futek, CA), and then multiplexed and delivered to the control board. The control board communicates wirelessly and provides a real-time control environment (Labview 2017, National Instruments, TX). Two custom-made printed circuit boards (Sunstone Circuits, OR), shown in Fig. 1.2, interface between the control board and the motors to

Figure 1.1: Robotic Spine Exoskeleton designed for female adolescents

drive the motors and multiplex potentiometer signals. The signals from the load cells are sent to a conditioning board (Mantracourt, ICA6H, UK) and then multiplexed with a custom circuit board. Another custom made circuit board regulates the voltage. Power to the control board is provided by a lithium polymer battery (7.4V, 2 Ah, Maxamps), and to the motors and other electronics by a lithium polymer battery (18.5 V, 4 Ah, Maxamps).

Adapting the design from [45] to the clinical population required three major adjustments. First, the top ring fits across the top of the sternum rather than at the bottom of the pectoral region and the center of the sternum. This improves the workspace for the top segment and provides a more comfortable fit for women. Second, the brace is cut from a flexible orthosis rather than printed in rigid plastic, and can fit a wider range of torso shapes. The brace opens at the back and is fastened with a spacer from a set ranging in width from 2 to 12 cm, shown in in Fig. 1.2. In addition to ensuring the rigidity of each ring, the spacers allow us to adjust the perimeter of each ring by 10 cm to accommodate a wide variety of torso shapes and sizes. These adjustments also affect the locations of the limb attachment points. The relative position of the limb attachment points for each size of spacer was measured with motion capture (Vicon Motion Systems, UK) to ensure the inverse kinematics was correct for all settings. The change in limb attachment positions

Figure 1.2: Robotic Spine Exoskeleton components. Top Left: ring spacing clasp. Bottom Left: Motor driver printed circuit board. Right: Motor housing.

can also modify the available range of motion. To counteract this, the motors are housed in custom-milled UHMW housings (Proto Labs, MN) shown in Fig. 1.2. These housings allow the rest length of the limb to be adjusted by up to 4 cm in 1 cm increments. Third, the torsos of adolescent are shorter and thinner than adult men, so the motors needed to be smaller, with a smaller offsets from the body as well. As an added benefit, this also reduced the weight of the device. Given these adjustments, our device was able to fit subjects with a torso height (minimum distance from iliac crest to axilla) of 20 cm to 35 cm, and with torso perimeter measuring 69-81 cm at the iliac crest level, 66-79 cm at the xyphoid level, and 67-85 cm at the axilla level. The brace weighs 3.28 kg and is capable of at least 0.16 rad of rotation about each axis and 20 mm translation in each direction for each combination of ring sizes.

The control system is as described in [45]. Each level of the RoSE can be controlled independently. There are two methods of control - position and force. Both methods are structured in two levels: a high-level controller that sets the desired motor outputs based on the the desired position or wrench, implemented at 200 Hz, and a low level controller that sets the pulse width modulation for each motor based on the desired length or force calculated by the high-level controller, implemented at 500 Hz. The built-in potentiometers of the linear actuators and the load cells in each limb provide the feedback for closed-loop control in either mode. The joint position/force

feedback is used to compute the real-time Cartesian position and forces on the brace levels. The controller's performance was validated on this hardware iteration using a motion capture camera system (Vicon Motion Systems, UK) and a six-axis force-torque sensor (Mini45, ATI Industrial Automation, NC).

Chapter 2: Torso Stiffness Characterization

In this chapter, we characterize the three-dimensional stiffness of the torso in vivo in adolescent females with and without scoliosis. First, we will present the collinear stiffness values, then the three-dimensional stiffness matrices, followed by the correlation matrices. The collinear stiffness values allow us to broadly compare the effects of group, torso segment, and degree-of-freedom on the stiffness of the torso. The three-dimensional stiffness matrices provide data that can be used to convert between a set of displacements on the torso, and the set of forces required to achieve it. Finally the correlation matrices allow us to see how tightly coupled force and displacement are in each combination of degrees-of-freedom.

2.1 Experiment protocol

Sixteen female adolescent subjects were recruited, eight with scoliosis (age 13.0 ± 2.1 years, height 157 ± 6 cm, weight 45.3 ± 9.3 kg) and eight without scoliosis (age 17.3 ± 0.7 years, height 162 ± 5 cm, weight 52.3 ± 4.9 kg). Informed consent was obtained from all subjects, and the study was approved by the Columbia Institutional Review Board. None of the subjects had a history of spine injuries, cardiopulmonary conditions, neurological or physical impairments, or other orthopedic impairments that might affect the spine and torso. The control group also did not have a history of back pain or spinal deformity. The subjects wore the brace while seated, and it applied small displacements to the torso, and measured the resulting force. The data collection protocol was similar to that described in [14], summarized and with differences noted here.

Subjects were measured and the brace was adjusted to their height and width. Any gaps between the body and the brace were filled with closed cell foam up to 3/8 inch thick. Subjects were comfortably seated on a stool throughout the data collection, and were instructed to relax and nei-

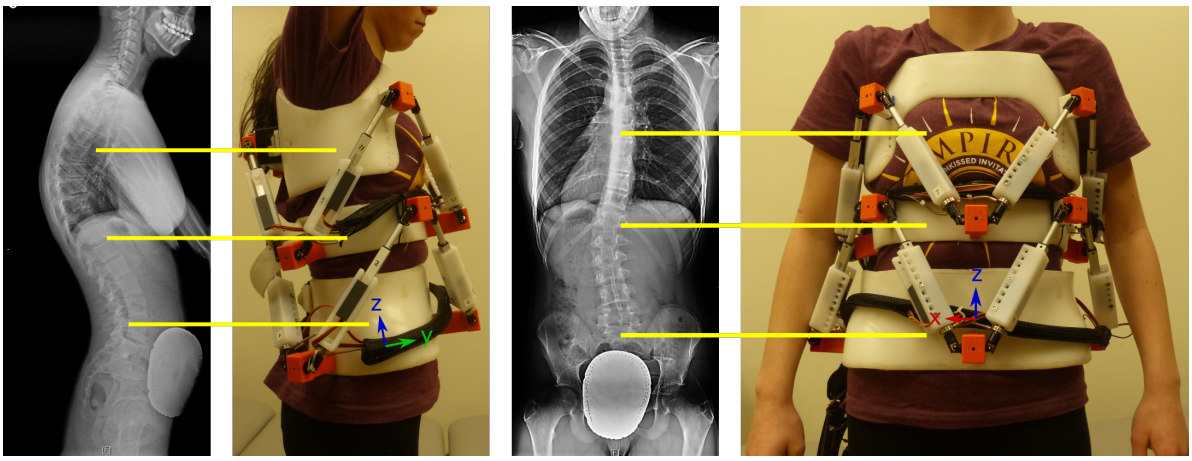

Figure 2.1: Left to Right: Out of brace sagittal plane radiograph; side view of the subject in RoSE; out of brace coronal plane radiograph; front view of the subject in RoSE. The subject is 13 years old, with a 25° left lumbar curve and a 16° right thoracic curve.

ther exaggerate nor resist the motion of the brace. A representative subject with scoliosis is shown in Fig. 2.1. Her out-of-brace radiographs are juxtaposed with images of her wearing the RoSE to illustrate the alignment of the device with the body.

Displacements were applied in two conditions: first, with the middle and top ring fixed relative to each other and moving together relative to the bottom ring; and second, with the bottom and middle ring fixed relative to each other and the top ring moving independently. For each condition, six displacements were applied in each degree-of-freedom. Displacement increments were determined by the subject's comfortable range of motion. Ideally, subjects received displacements of -15, -10, -5, 5, 10 and 15 mm in translation, and -0.15, -0.10, -0.05, 0.05, -0.10, and -0.15 radians in rotation. However, if the subject expressed discomfort at the extremes of this range, the displacements were reduced to -12, -8, -4, 4, 8, and 12 mm in translation, or -0.12, -0.08, -0.04, 0.04, 0.08, and 0.12 radians in rotation. The actual position was recorded simultaneously with the force and moment data and used for analysis. Three cycles of displacement were performed at each of the displacement positions, and the mean of the measured force and displacement was used for the analysis. A displacement cycle consisted of 1 second of translation to the new position, 2 seconds of maintaining the position and recording the resultant forces and moments, 1 second of data collection, 1 second of returning to the neutral position, and finally a 1 second pause before be-

ginning the next cycle. During the one second data collection, both position and forces/moments were recorded at 100 Hz. During the pause in the neutral position, the load cells were tared so that residual forces and moments would be accounted for. The data collection is shown in the accompanying supplementary video.

2.2 Data Analysis

To see whether our control and scoliosis groups differed in any significant way other than spinal condition, we used a 2 sample t-test to determine whether the groups were significantly different in terms of age, height, or weight. The data was then analyzed to determine whether the force was linearly related to the displacement. To do this, we calculated the adjusted coefficent of determination (adjusted r-squared value) for the collinear force-displacement plot for each subject.

After confirming that the assumption of linear stiffness held for this group, we computed the collinear stiffness values in each dimension for both groups. The distribution of collinear stiffness values was tested for normality using the Shapiro-Wilk tests. A three way mixed model Analysis of Variance (ANOVA) with two between factors (group: control and scoliosis; thorax level: upper and lower) and one within factor (degree-of-freedom: x, y, and z) was applied. This model was applied separately to translational and rotational degrees-of-freedom. Leven's and Mauchly tests were used to explore variance and Sphericity of data. Greenhouse-Geisser correction was used in case sphericity assumption was violated. The significance level was set at an alpha rate of 0.05. Posthoc testing was analyzed only if the ANOVA model was significant (omnibus test). Bonferroni's inequality procedure was applied to adjust p-values and control the familywise error rate. Additionally, the statistical power of the ANOVA models are addressed in case of statistical significance.

We then constructed the three-dimensional stiffness matrix for each subject, non-dimensionalized and normalized it, and then found the mean and standard deviation across the group. Next, we re-normalized and re-dimensionalized the group stiffness matrix to retrieve its real-world significance. This process is detailed in [14] and summarized in the appendix. Each term in the normalized stiff-

Table 2.1: Adjusted Coefficient of Determination for Collinear Stiffnesses

	Control		Scoliosis	
	Lumbar	Thoracic	Lumbar	Thoracic
k_x	0.97 ± 0.05	0.98 ± 0.03	0.97 ± 0.04	0.94 ± 0.07
k_y	0.99 ± 0.01	0.99 ± 0.01	0.99 ± 0.01	0.99 ± 0.01
k_z	0.97 ± 0.02	0.97 ± 0.01	0.97 ± 0.01	0.94 ± 0.06
k_ϕ	0.87 ± 0.22	0.89 ± 0.11	0.95 ± 0.07	0.91 ± 0.13
k_θ	0.93 ± 0.08	0.94 ± 0.11	0.94 ± 0.04	0.96 ± 0.03
k_ψ	0.91 ± 0.07	0.94 ± 0.05	0.94 ± 0.04	0.97 ± 0.02

Table 2.2: Group Collinear Stiffnesses

	Control		Scoliosis	
	Lumbar	Thoracic	Lumbar	Thoracic
k_x [N/m]	1416 ± 74	1217 ± 79	1205 ± 86	1199 ± 128
k_y [N/m]	1600 ± 89	1542 ± 89	1885 ± 59	1669 ± 67
k_z [N/m]	2812 ± 65	2378 ± 51	3286 ± 198	3270 ± 128
k_ϕ [Nm/rad]	21 ± 2	17 ± 2	38 ± 1	32 ± 4
k_θ [Nm/rad]	18 ± 1	21 ± 2	38 ± 3	43 ± 2
k_ψ [Nm/rad]	17 ± 1	17 ± 1	33 ± 2	32 ± 2

ness matrix was tested for normality using the Shapiro-Wilkes test. Each term was then tested for significant difference from zero using either a one-sample t-test or Wilcoxon signed rank test depending on whether the distribution was normal.

2.3 Results

2.3.1 Collinear Stiffnesses

For both groups at both levels of the trunk, there existed a strong linear relationship between force and displacement. The linear model was a good fit, with an adjusted coefficient of determination of at least 0.87 for every direction in each group and level. Average adjusted coefficient of determinations are reported for each DOF in Table 2.1. The two groups had significantly different mean ages (2 sample t-test with unequal variance, p = 0.006). The groups did not have significantly different heights or weights. We then tested whether age correlated with collinear stiffness in any degree-of-freedom at either segment of the torso. We found that the age was only signifi-

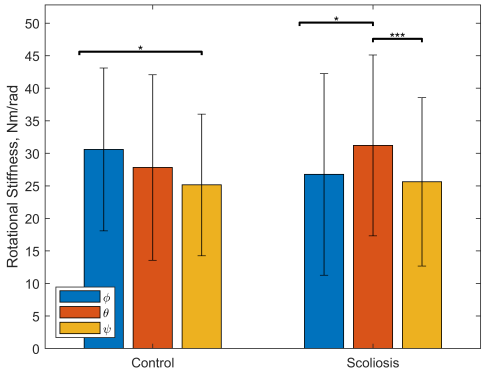

Figure 2.2: Rotational stiffness for combined thoracic and lumbar levels in control and scoliosis groups. Bars show significant differences between groups (* represents $p < 0.05$, ** represents $p < 0.01$, and *** represents $p < 0.001$)

cantly correlated with collinear stiffness in the y-direction at the thoracic segment (p=0.013), and increased on average 78 N/m per year. However, due to the fact that only one outcome out of twelve was correlated with age, we did not analyze its effects further.

The mean collinear stiffness values are given in Table 2.2. The Shapiro-Wilk test for normality indicated that distribution was normal for all groups and directions, except the control group in the x-direction of the lumbar region and the y-direction of the thoracic region, and for the scoliosis group in the z-direction of the lumbar region. During translations, the statistical analysis showed an interaction effect between DOF and torso segment on stiffness ($F(1.6, 44.98) = 11.77$, $p = 0.000$, power = 0.72). Significant differences in stiffness between lumbar and thoracic regions were observed within y-translation (Thoracic = 1764 (SD:316), Lumbar = 1548 (SD:162), $p = 0.02$) and within z-translation (Thoracic = 3253 (SD:589), Lumbar = 2623 (SD:550), $p = 0.02$). This differs from observations on the stiffness in adult males, in which the lumbar region had greater stiffness for all degrees-of-freedom. Within either lumbar or thoracic segments, all DOFs were different with respect to each other. The relative magnitudes of the translational stiffnesses, $k_x < k_y < k_z$, were generally in line with prior research on the human spine segments [46, 47, 48, 49], but differed somewhat from the relative torso stiffnesses of adult males[14], which was $k_y < k_x < k_z$.

During rotations, an interaction effect between DOF and group for stiffness was found ($F(2,$

56) = 3.70, p = 0.031, power = 0.66). No differences in stiffness were found between control and scoliosis groups (ϕ rotation, p = 0.334; θ rotation, p = 0.348, and ψ rotation, p = 0.882). However, the DOFs were significantly different within groups, as shown in Fig. 2.2, in differing patterns between the scoliosis and control groups.

Overall, the stiffness of the torso was about two orders of magnitude smaller than the spine itself in translational degrees-of-freedom, but about one order of magnitude less stiff in the rotational degrees-of-freedom [46, 47, 48, 49]. It is also somewhat lower than the torso stiffness of adult males measured in [14]. This difference is consistent with findings that adult male spinal disks have greater compressive stiffness than adult female spinal disks in vitro [50]. Males would be expected to have more well developed musculature than females, which would be expected to increase stiffness as well. Age may also play a role, as changes to the skeleton and muscles during maturation could affect the torso stiffness.

2.3.2 Stiffness Matrices

The three-dimensional stiffness characterization for each group at each level is presented in Fig. 2.3. The 6×6 stiffness matrices contains the collinear stiffness terms along the diagonal and the coupling stiffness between different degrees-of-freedom in the off-diagonal terms. As expected, the group average stiffness matrices were not symmetric. This is in agreement with properties observed in human spine segments [51], as well as in adult male torsos [14], and is supported by the fact that spine, ligaments, muscles, and other soft tissues have some viscous properties, in addition to potential nonconservative contributions to the force provided by contact forces in the facet and costovertebral joints, and activation forces from the muscles and ligaments in the torso.

2.3.3 Correlation Matrices

Kendall's rank correlation coefficient was calculated to assess the correlation between forces and displacements in all directions, shown in Fig. 2.4. Kendall's was preferred to Pearson's rank correlation coefficient because the distribution of displacements did not follow a normal distribu-

	Tx	Ty	Tz	Rx	Ry	Rz
Fx	1205 ±86	-25 ±51	-90 ±70	-28 ±14	-194 ±16	-25 ±11
Fy	74 ±48	1885 ±59	105 ±193	181 ±26	-14 ±10	-45 ±17
Fz	51 ±54	-31 ±120	3286 ±198	63 ±17	7 ±12	15 ±8
Mx	-2 ±6	208 ±14	86 ±12	38 ±1	3 ±2	-1 ±2
My	-97 ±5	-9 ±5	15 ±17	3 ±2	38 ±3	5 ±2
Mz	-25 ±12	-31 ±10	36 ±12	-2 ±2	2 ±3	33 ±2

(a) Control Group, Thoracic

	Tx	Ty	Tz	Rx	Ry	Rz
Fx	1199 ±128	-141 ±57	8 ±66	-40 ±8	-139 ±10	-8 ±18
Fy	17 ±48	1669 ±67	242 ±73	140 ±14	5 ±9	-59 ±13
Fz	72 ±38	60 ±44	3270 ±128	51 ±16	26 ±17	26 ±9
Mx	-20 ±6	172 ±8	23 ±21	32 ±4	4 ±1	-6 ±1
My	-77 ±4	19 ±7	23 ±9	2 ±1	43 ±2	4 ±2
Mz	-28 ±8	-43 ±11	29 ±19	-3 ±2	-0 ±2	32 ±2

(b) Scoliosis Group, Thoracic

	Tx	Ty	Tz	Rx	Ry	Rz
Fx	1416 ±74	78 ±38	139 ±62	-6 ±6	-56 ±10	-6 ±7
Fy	11 ±35	1600 ±89	57 ±98	92 ±10	14 ±5	-8 ±7
Fz	202 ±40	8 ±70	2812 ±65	34 ±21	-2 ±5	5 ±7
Mx	-7 ±5	82 ±8	30 ±20	21 ±2	-1 ±1	-2 ±1
My	-50 ±8	9 ±3	-23 ±3	0 ±1	18 ±1	4 ±1
Mz	-21 ±8	-11 ±3	-8 ±7	0 ±1	2 ±1	17 ±1

(c) Control Group, Lumbar

	Tx	Ty	Tz	Rx	Ry	Rz
Fx	1217 ±79	8 ±49	-129 ±80	-9 ±8	-36 ±18	-2 ±7
Fy	21 ±46	1542 ±89	-13 ±45	75 ±6	9 ±5	-9 ±5
Fz	26 ±56	-75 ±49	2378 ±51	20 ±16	4 ±7	13 ±7
Mx	-6 ±5	73 ±5	21 ±14	17 ±2	-1 ±1	-1 ±1
My	-33 ±4	6 ±5	-26 ±9	-0 ±0	21 ±2	3 ±1
Mz	-23 ±5	-6 ±4	-5 ±12	-0 ±1	2 ±1	17 ±1

(d) Scoliosis Group, Lumbar

Figure 2.3: Mean ± the standard deviation of the rescaled stiffness matrices by group and torso segment. Stiffness matrices for the thoracic level are shown in (a) and (b), while the lumbar level is shown in (c) and (d). The average stiffness matrices for the control group are shown in (a) and (c), while (b) and (d) show the averages for the scoliosis group. The upper left quadrant of each matrix has the unit [N/m], the upper right and the lower left quadrants have the unit [N], and the bottom right quadrant has the units [Nm/rad].

tion for all degrees-of-freedom. Correlations that are statistically different from zero are marked with asterisks (* $p < 0.05$, ** $p < 0.01$). The diagonal terms of each matrix are the collinear force-displacement relationships, and are strongly correlated for both groups at both levels, as expected.

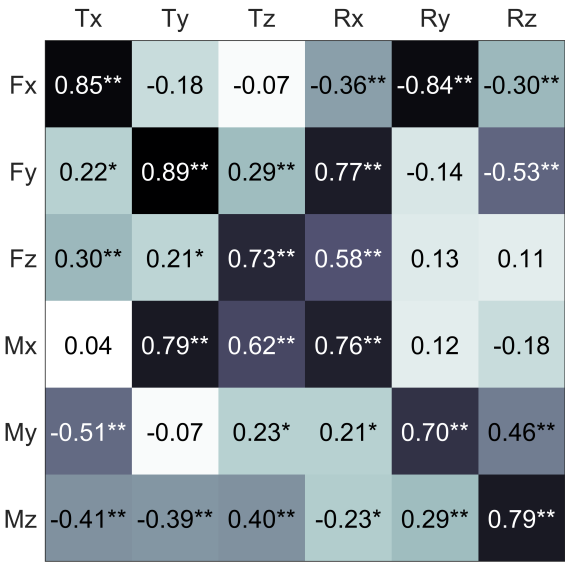

(a) Control Group, Thoracic

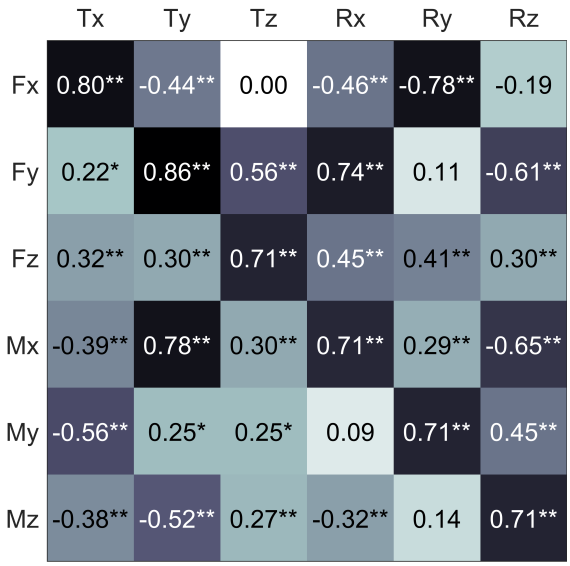

(b) Scoliosis Group, Thoracic

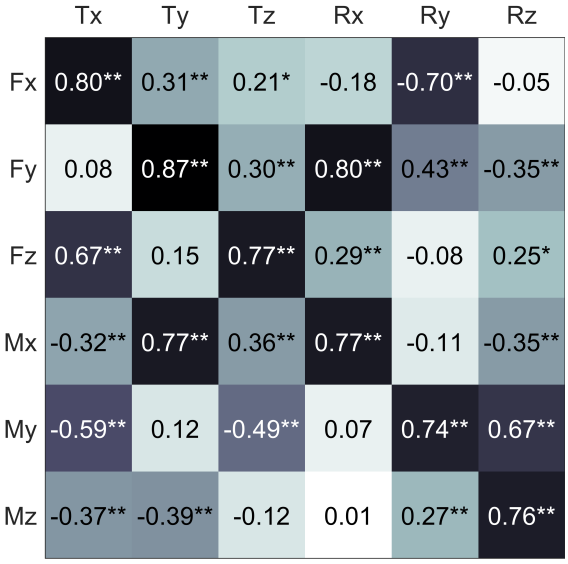

(c) Control Group, Lumbar

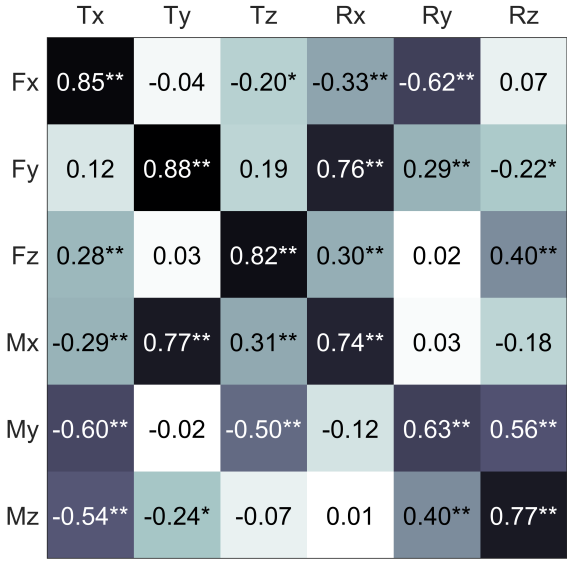

(d) Scoliosis Group, Lumbar

Figure 2.4: Correlation matrices by group and torso segment. The correlation matrices for the thoracic level are shown in (a) and (b), while the lumbar level is shown in (c) and (d). The correlation matrices for the control group are shown in (a) and (c), while (b) and (d) are for the scoliosis group. Asterisks mark correlations that are significantly different from zero ($*p < 0.05$, $**p < 0.01$). Cell shading is on a gradient from weakest correlation (white) to strongest correlation (black).

Many of the off-diagonal terms are also strongly correlated, particularly terms k_{51}, k_{42}, k_{24}, and k_{15}. This set of terms is referred to as the primary coupling, and would be expected due to the pelvis being fixed. For example, in k_{51}, translating the torso in the x-direction relative to the pelvis

would be expected to create a lateral bending moment. This set of couplings is strong ($\tau > 0.5$) for both groups and both levels, and can also be found in the stiffness matrix of the spine itself [49].

Some additional off-diagonal terms show strong correlations in one or more of the groups and levels. For the control group, this is k_{26}, k_{34}, and k_{43} at the thoracic level and k_{31} and k_{56} at the lumbar level. For the scoliosis group, this is k_{23}, k_{26}, k_{46} and k_{62} at the thoracic level and k_{53} and k_{56} at the lumbar region. Some of these couplings, for example, $k_{23}, k_{34}, k_{43}, k_{56}$ and k_{61}, may be due to the posterior displacement of the spine, which is the stiffest element in the torso. For example, a displacement applied in the x-direction may displace the ribs and center of the torso more easily than the spine at the back of the torso, and thereby create a moment about the z-axis (k_{61}). Finally there may be some additional strong correlations that relate to the curves in the spine itself. In the thoracic region, both groups have a strong correlation at k_{26}. In the lumbar region, the correlation in k_{53} could be related to the natural lordosis of the lumbar spine flattening out during extension. In the scoliosis group, the terms k_{46} in the thoracic region is an out of plane coupling that may be due to the scoliotic curve.

2.4 Discussion

2.4.1 Clinical Implications

We found that collinear stiffnesses of the female adolescent torso to be similar to the human spine in terms of relative magnitude, although lower in magnitude overall. In addition, the collinear stiffness were not significantly different between the two groups, although there was an interaction effect between the group and the DOF in the rotational stiffness. This indicates that it may be relatively more difficult for someone with scoliosis to bend laterally than to bend in flexion/extension, as compared to someone without scoliosis. We found that the three dimensional coupling stiffness characteristics of the torso are comparable to those of the human spine, irrespective of AIS. While it might be assumed that this type of spinal deformity would create significant changes in the population in terms of the collinear stiffnesses or the coupling stiffness characteristics, AIS is a highly individualized disorder. Individual differences may be more salient than generalized comparison

between the AIS population as a whole and the typically developing population.

The findings also suggest that the torso stiffness of female adolescents is different in magnitude from that of adult males. The differences between this population and those previously studied underscore the importance of using data gathered from this group in order to design interventions intended for them. Overestimating the torso stiffness could result in brace designs that apply too much force and create discomfort or injury.

2.4.2 Applications

This data provides a benchmark which could be used for validating FEM models of the torso. In particular, it provides a helpful frame of reference for working with adolescent patients, who are not well represented in prior work on the spine in vitro or the torso in vivo, and who may have different material properties of the torso than adults. In addition, these results can inform the design of scoliosis braces. The stiffness matrix allows one to calculate the effects of forces and moments applied in multiple directions on rotation and displacement of the torso, and vice versa. This can allow rigid orthoses manufacturers to better understand the amount of force applied to the torso by a given orthosis design. For the manufacturers of flexible orthoses, the stiffness matrix data can help them better estimate the amount of tension needed in straps to ensure that sufficient correction is achieved, as well as improve the placement of the straps. Finally, the device and methodology presented provide a strategy for quickly and easily obtaining detailed data on the stiffness characteristics of an individual without subjecting them to radiation, which could be incorporated into the design of individualized scoliosis braces in the future.

2.4.3 Limitations and Future Work

The results of this study shed light on the stiffness of the torso in female adolescents and the forces/moments required to create specific displacements. However, to truly understand how forces applied to the torso affect the displacement of the spine, it is necessary to image the spine itself during these procedures. Such technology is available in the form of EOS imaging systems, which

use low-dose dual-plane x-rays to reproduce the 3D position of the spine with a fraction of the radiation of a traditional chest x-ray. In addition, the study was restricted to quasi-static analysis of the torso stiffness. However, the dynamic properties of the torso may also be of interest, because the soft tissues of the torso do not behave in a purely elastic way.

In this study, there was a difference in the mean age of the two groups. However, within each group, there was no significant correlation between age and collinear torso stiffness terms at the upper or lower level of the torso, which allowed us to neglect age in our analysis. Adolescence is a period of rapid change, and it may be possible that there is an effect of age that we were unable to detect. Further, we did not have a way to measure skeletal maturity, a factor correlated with age but which has a strong influence on the likelihood of progression in scoliosis, and which would be expected to affect spinal stiffness. It may be informative to run a longitudinal study to see how individual's torso properties change over time in this population, and to correlate that with a metric of skeletal maturity, such as the Risser sign.

Another limitation on the present study is that the relationship between torso stiffness and muscle activation is not well understood. We were unable to capture this aspect through surface electromyography because of the limited surface area of the torso on which electrodes could be placed while the device was worn. This area is further reduced during bending, and the procedure entailed bending in every direction. Therefore, there were no locations suitable to place electrodes on the user during the experiment. To provide consistency in this experiment, subjects were instructed to relax as much as possible. However, if were possible, it may be useful to measure how the muscles activate in response to forces applied to the torso, and how that affects the measured stiffness.

Despite the limitations present, the stiffness characterization can enable us to use the RoSE to study physical therapy interventions in posture rehabilitation. For example, we can design paradigms that allow us to apply a corrective force in some degrees-of-freedom, and anticipate the effects of that force on posture change both in the desired degree-of-freedom and other directions as a result of stiffness coupling. We could modulate these forces as subjects move through a

variety of postures in order to encourage them to recognize a range of desirable postures rather than one static pose. Alternatively, we could apply forces opposite to the direction of desired direction of displacement, in order to train the subject to resist and strengthen their muscles.

2.5 Conclusion

In this section, we use the RoSE to characterize the stiffness of the torso in eight female adolescents with scoliosis, and eight without. The key findings include the collinear stiffnesses, which had an interaction effect between torso segment and degree-of-freedom in translation and between group and degree-of-freedom in rotation; and the three dimensional coupling stiffness characteristics of the torso, which are comparable to those of human spine, irrespective of spinal deformity. This data can be used to validate FEM models of the torso and inform the design of scoliosis braces.

Chapter 3: Sensory Feedback and Torso Motor Learning

In this chapter, we first studied the impact of sensory feedback on the ability of adolescent girls to replicate a desired static posture. We compared the effect of augmented visual feedback to augmented somatosensory feedback provided by gentle forces from the RoSE. In order to see whether these results persisted in a more complex motor learning tasks, we then compared these types of augmented sensory feedback on learning a dynamic posture movement.

3.1 Static Posture Training

Informed consent was obtained from eight subjects, none of whom had any neuromotor impairment. Subjects were divided into two groups of four. One group (n=4) received visual feedback and the other group (n=4) received force feedback. Each subject was asked to learn six target poses (flexion, extension, lateral bending right, lateral bending left, axial rotation clockwise, axial rotation counterclockwise). For each target pose, the subject was given three attempts to achieve the pose with the aid of the feedback. The subject started each attempt from the neutral pose, and notified the experimenters when they felt that were as close as they could get to the desired pose. They maintained the position for three seconds, and then the brace was switched to position control, returning them to the neutral pose. Once they had completed three attempts of training with the feedback, they were given a 30 second break and then asked to replicate the target pose without the aid of the feedback (testing). The subjects had three attempts to demonstrate the target pose during the testing phase. Each attempt, whether during testing or training, was stopped at two minutes even if the subject had not stated that they had reached the target pose.

Visual feedback was provided through a Labview GUI, which displayed an avatar as shown in Figure 3.1. Each segment of the RoSE was represented by two colored blocks. The dark colored

Figure 3.1: Subject completing the static posture task with visual feedback

blocks represented the segment in the target pose, and the light colored blocks represented the segment in the current pose (obtained from the RoSE). The subject's goal was to find the torso pose that exactly aligned the light blocks with the dark blocks.

Force feedback was provided through impedance control with the RoSE itself. The device acted as a virtual spring centered at the target pose. It provided no force/moment at the target, but outside it, provided a force/moment towards the target that was linearly proportional to the displacement from the target. This is similar to the assist-as-needed control strategy used in many upper or lower limb rehabilitation devices. The subject's goal was to find the torso pose that minimized the amount of force they felt.

A two-way ANOVA was run to examine the effect of feedback and pose on rotational error during training in the lower and upper levels. For the lower level, the force feedback group had significantly less error than the visual feedback group (p=13.8e-10), but there was no significant effect of pose. For the upper level, the force feedback group again had significantly lower error (p = 1.5e-10), but there was also a main effect of pose (p = 1.0e-06).

This suggests that subjects were better able to identify the correct pose with the help of the force feedback, although some poses may have been more difficult than others. For example, extension in the thoracic region may have been difficult.

To see how the training effects carried over after the feedback was removed, a two-way ANOVA was run to examine the effect of feedback and pose on rotational error in the lower and upper levels during testing. For the lower level, the force feedback group had significantly less error than the visual feedback group (p=0.0020), but there was no significant effect of pose. For the upper level, the force feedback group was not significantly different from the visual feedback group (p = 0.13), but there was a main effect of pose (p = 0.036). This suggests that, at least at the lumbar level, subjects were able to replicate the pose they had learned before with the help of the force feedback. At the thoracic level, though, the relative merits of each type of feedback is more nuanced. In particular, the subjects who had received force feedback struggled with flexion/extension of the thoracic region, and excelled at axial rotation, whereas the visual group performed similarly across

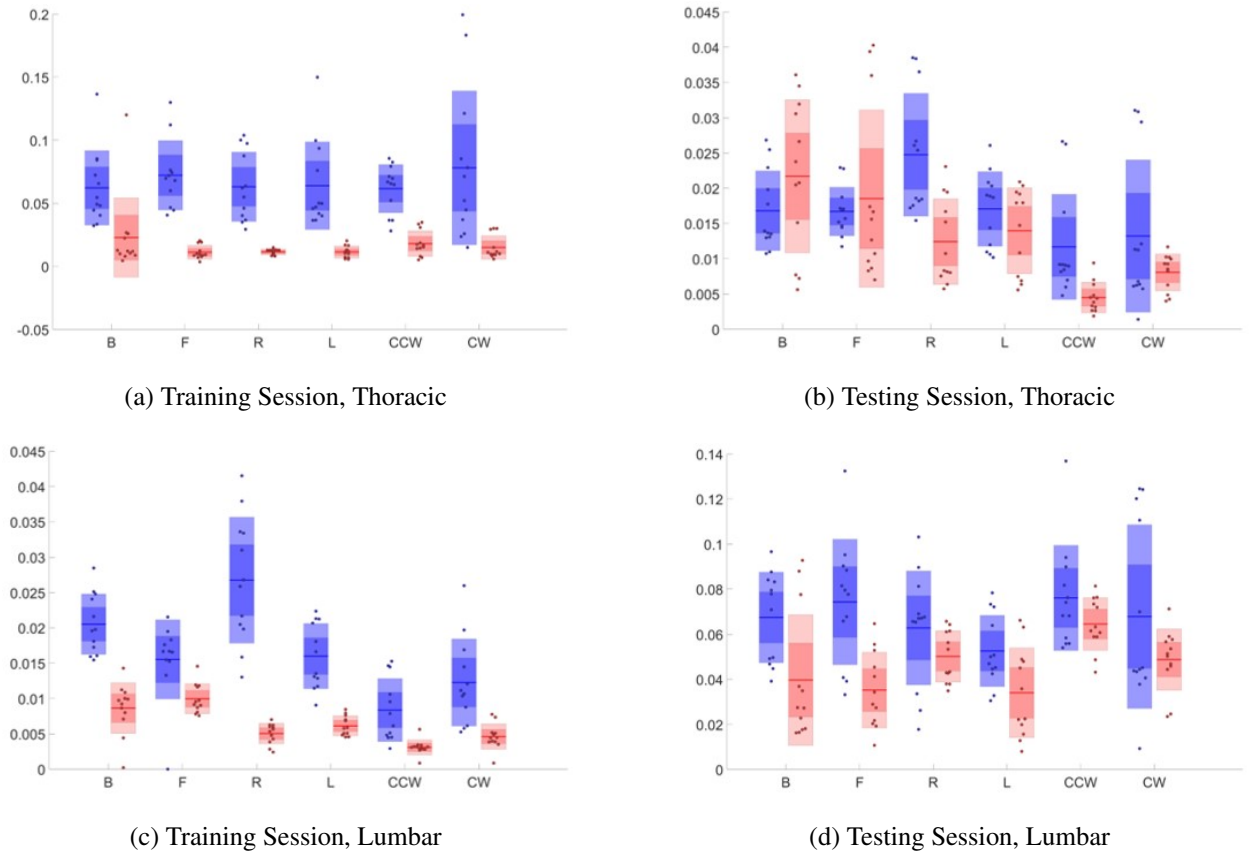

(a) Training Session, Thoracic

(b) Testing Session, Thoracic

(c) Training Session, Lumbar

(d) Testing Session, Lumbar

Figure 3.2: Rotational error during static posture training and testing. Data from the visual feedback group is shown in blue, and data from the force feedback group is shown in red. Plots (a) and (c) show error during training, while (b) and (d) show error during testing. Pl ots (a) and (b) are from the thoracic level, while plots (c) and (d) are from the lumbar level. Error values of individuals are represented by points, while the group mean error is shown as the center line. The lightly shaded box represents the one standard deviation of the mean, and the heavily shaded inner box represents 95% confidence interval of the mean.

degrees of freedom.

3.2 Dynamic Posture Training

In physical therapy for scoliosis, after a patient is able to master spinal alignment in a static posture, they being to learn how to maintain healthy alignment while moving through a torso trajectory, such as bending forward, or walking [26]. In this stage, too, the clinician may continue to provide augmented sensory feedback until the patient is able to maintain a healthy alignment throughout the movement. However, this task is even more complex than static challenge, and the

optimal sensory feedback strategy may differ from the static task. For this reason, we decided to explore the effects of visual and somatosensory feedback on dynamic posture training.

In this study, a torso trajectory was defined as a sequence of torso postures. The trajectories were chosen because they feature challenges in terms of segmenting trunk movement, and coordinating rotation about multiple axes, that are essential to scoliosis physical therapy. The first trajectory was flexion and extension of the torso in the sagittal plane. The challenge for the subjects was to separately articulate the lumbar and thoracic regions of the torso. The subjects first needed to flex the thoracic region, then flex the lumbar, then straighten the thoracic region, and finally straighten the lumbar region. This movement is similar to a "body roll", commonly performed in Afro-Caribbean dance styles. The second trajectory consisted of lateral bending as well as forward bending, and the challenge for the subjects was to combine multiple degrees of freedom in a complex, out-of-plane motion. For this trajectory, the subjects moved both segments of the torso together. The subjects need to bend laterally first, then flex forward while maintaining the lateral bend (this also introduced a slight axial twist). The subjects then unbent the lateral degree of freedom (at which point they were bending forward). Finally, they straighten to upright standing. This movement is similar to a "grande port des bras" featured in ballet dance. Within their respective dance styles, both of these movements are known to be difficult, yet achievable with practice, indicating that they would provide a suitable challenge for a healthy subject.

The augmented visual feedback provided consisted of an avatar depicting the desired position and the actual position, as shown in figure 3.3. The subject was shown this avatar from two different views. By default, the views shown were the back view and right side view, although either view could be rotated at the subject's request.

The augmented somatosensory feedback consisted of a virtual force field around the desired pose. The wrench, $\boldsymbol{f}$, applied to the subject was proportional to the difference between the desired pose, $\boldsymbol{x_{des}}$, and their actual pose, $\boldsymbol{x_{act}}$, and calculated as:

$$\boldsymbol{f} = \boldsymbol{K}(\boldsymbol{x_{des}} - \boldsymbol{x_{act}})$$

$$\begin{bmatrix} k_T & 0 & 0 & 0 & 0 & 0 \\ 0 & k_T & 0 & 0 & 0 & 0 \\ 0 & 0 & k_T & 0 & 0 & 0 \\ 0 & 0 & 0 & k_R & 0 & 0 \\ 0 & 0 & 0 & 0 & k_R & 0 \\ 0 & 0 & 0 & 0 & 0 & k_R \end{bmatrix} \left(\begin{bmatrix} x_{des} \\ y_{des} \\ z_{des} \\ \phi_{des} \\ \theta_{des} \\ \psi_{des} \end{bmatrix} - \begin{bmatrix} x_{act} \\ y_{act} \\ z_{act} \\ \phi_{act} \\ \theta_{act} \\ \psi_{act} \end{bmatrix} \right) = \begin{bmatrix} f_x \\ f_y \\ f_z \\ \tau_\phi \\ \tau_\theta \\ \tau_\psi \end{bmatrix}$$

Where the spring constants for the translational degrees of freedom, k_T and rotational degrees of freedom, k_R were 100 and 500 respectively. Since the intention was not to restrict translational motion, in initial testing a spring constant of 0 was applied. However, this made it difficult for the user to achieve any rotations, because the brace segments would slide instead. The additional stiffness made it easier for the user to achieve the desired rotations without overly restricting the translation.

Informed consent was obtained from five subjects. Three subjects were assigned to the force group and two to the visual group. The subjects were female young adults between ages 18 and 35, with no history of scoliosis or neuromotor impairments.

After being fitted with the brace, the brace was put into zero-force mode, and the subjects stood upright in a comfortable position. This position was recorded and used as the home position, which started and ended every trajectory. Next, they were as to move through their full range of motion in flexion/extension, lateral bending, and axial rotation. This data was used to calculate each subject's

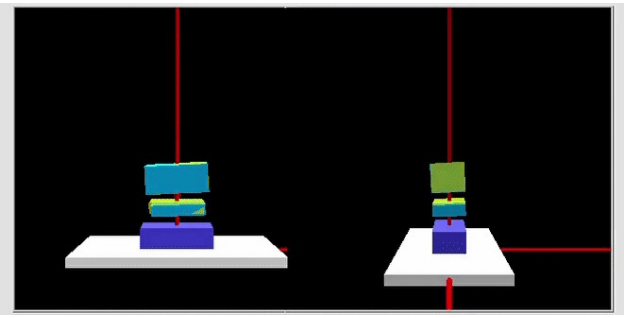

Figure 3.3: Avatar displayed during visual feedback

personalized trajectories. The degree of rotation between successive poses within a trajectory was 0.01 radians or less.

The subjects then attempted to learn the two trajectories. The subjects were given 5 attempts to learn each trajectory with the help of the feedback. Next, they were given 5 attempts to demonstrate the trajectory as they understood it. They were given several attempts to demonstrate the trajectory in order to distinguish genuine misunderstanding of the desired movement as compared to difficulty replicating the movement with precision.

3.2.1 Data analysis

Brace position and and applied force were recorded at 10 Hz. The data was first analyzed to see what phase of the trajectory the subject was in at each point in time. To do this, the derivative of the position was calculated at each time point, and the data points were then classified into five categories, as shown in figure 3.4a and 3.4b. The first four categories corresponded to each of the four quadrants of a the desired trajectory. The fifth category corresponded to movement that was not characteristic of any quadrant of the trajectory. Data in this category could indicate an exploratory movement of the subject during the training phase, or it could indicate a fundamental misunderstanding of the trajectory during the testing phase.

Figure 3.5 shows the time spent in each phase of the flexion trajectory, for both groups. During

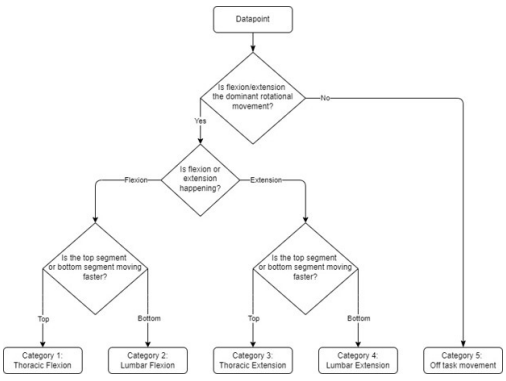

(a) Flexion Trajectory Data Classification

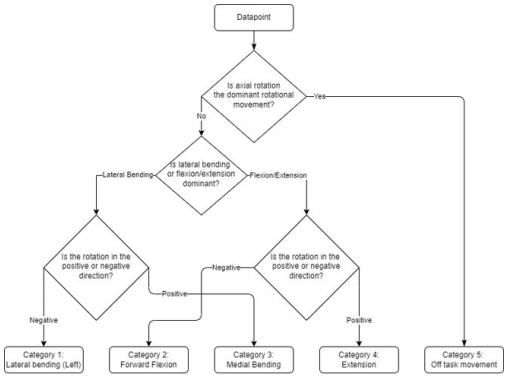

(b) Compound Trajectory Data Classification

Figure 3.4: Data classification algorithms for the flexion and compound movement trajectories.

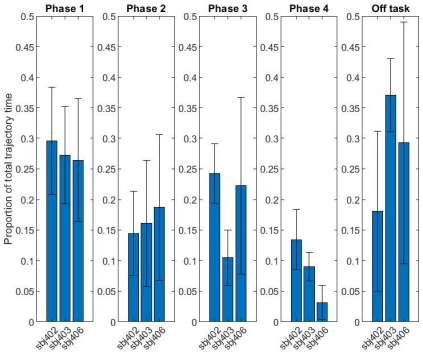

(a) Flexion Trajectory Phases During Training Sessions, Force Group

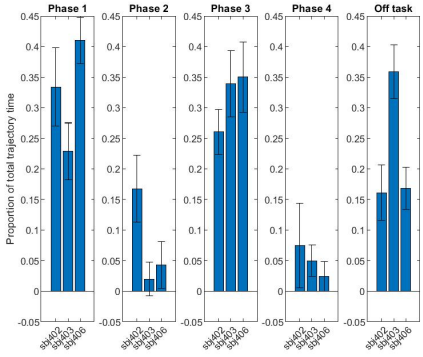

(b) Flexion Trajectory Phases During Testing Sessions, Force Group

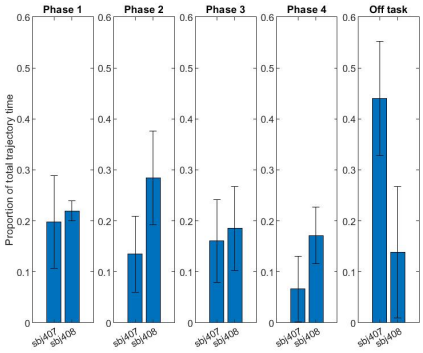

(c) Flexion Trajectory Phases During Training Sessions, Visual Group

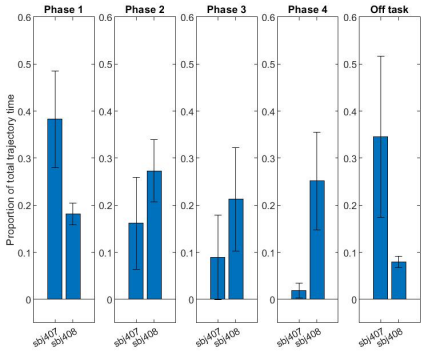

(d) Flexion Trajectory Phases During Testing Sessions, Visual Group

Figure 3.5: Proportion of time spent in each phase of the flexion trajectory.

the flexion trajectory, the force group spent a similar amount of time in all four phases of the trajectory during the training sessions, and about 30% of the time on off-task movement. During testing, they spent about 20% of their time on off-task movement. This suggests that they were able to recognize some of their exploratory movements from the training session were not part of the target trajectory and discard them, resulting in a more streamlined movement. However, they also spent far more time in phases one and three of the trajectory than in phases two and four. This suggests that the subjects did not correctly identify the segment isolation aspect of the target trajectory, and relied on flexion of the top segment of their torso rather than the lower segment. Performance was relatively similar among the three group members.

In contrast, the visual feedback group members performance was more disparate. During train-

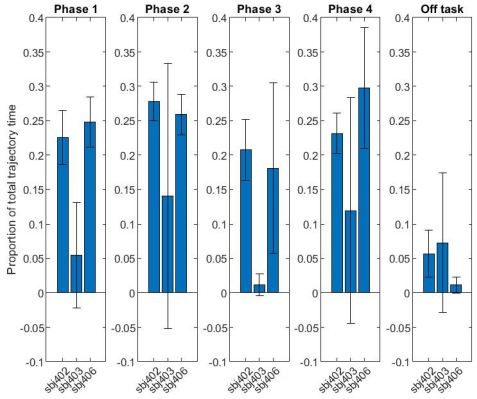

(a) Compound Trajectory Phases During Training Sessions, Force Group

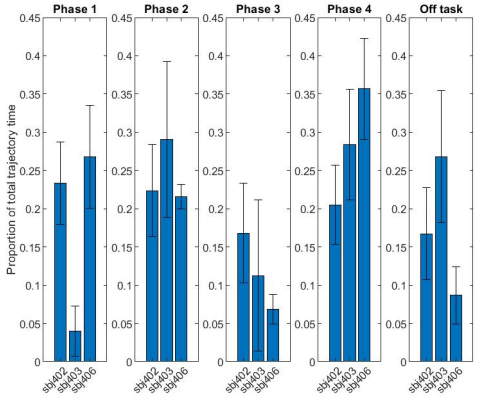

(b) Compound Trajectory Phases During Testing Sessions, Force Group

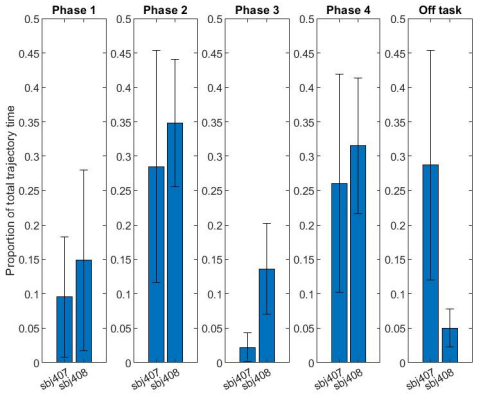

(c) Compound Trajectory Phases During Training Sessions, Force Group

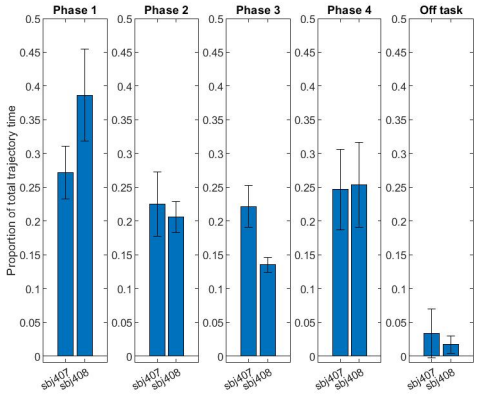

(d) Compound Flexion Trajectory Phases During Testing Sessions, Visual Group

Figure 3.6: Proportion of time spent in each phase of the compound trajectory.

ing, both subjects spent approximately equal time on all four phases of the trajectory, but one subject spent nearly 45% of the time on off-task behaviour while the other spent less than 15%. For the testing sessions, both subjects reduced the amount of time spent on off-task movements. One subject spent approximately equal time on the four phases, suggesting that she was able to correctly identify and articulate the top and bottom segments. The other spent less time on each successive phase. This may indicate that she learned the beginning phases of the trajectory better than the later ones.

For the compound trajectory, the force group had a roughly balanced four phases in both training and testing sessions. However, the amount of time spent in off-task movements increased from

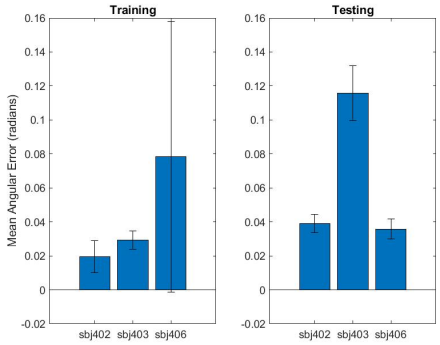

(a) Flexion Trajectory Mean Angular Error During Training Sessions, Force Group

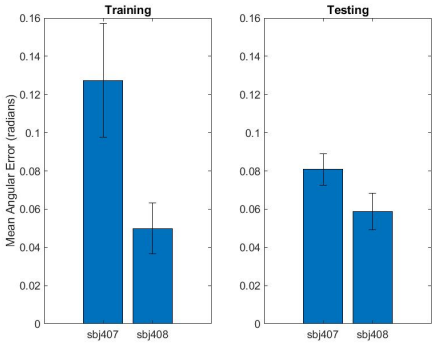

(b) Flexion Trajectory Phases During Testing Sessions, Visual Group

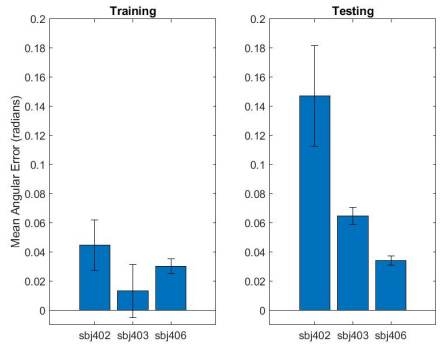

(c) Compound Trajectory Mean Angular Error, Force Group

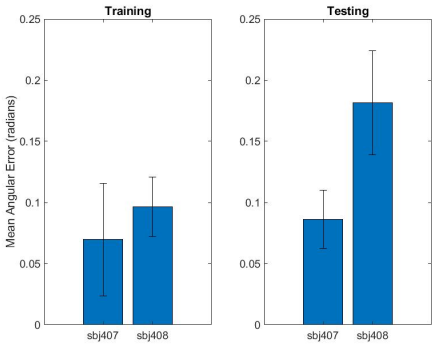

(d) Compound Trajectory Mean Angular Error, Visual Group

Figure 3.7: Mean angular error during on-task phases of the trajectory for the force and visual feedback groups.

training to testing, from approximately 4% to 20%. The visual group had less time in phase one and three than two and four in the training phase, but roughly equal amounts of time in the testing phase. The amount of time spent on off-task behaviours also decreased from training to testing.

In addition to time in each phases, I also analysed the average error in position throughout the on-task phases of the trajectory, as well as the coordination error, which takes into account the two most important degrees of freedom of the trajectory.

For the flexion trajectory, results were highly individualized, with some subjects having greater error during the training sessions and others during the testing sessions. The visual group had slightly higher error in both sessions. For the compound trajectory, both groups tended to have greater mean angular error during the testing sessions than the training sessions. This indicates

that they were not able to replicate the trajectory as accurately without the help of the feedback. The error was higher in the visual group for both sessions.

Finally, I calculated the coordination error, a metric which combines the error in the two main degrees of freedom. This is analogous to the error in the main degree of freedom in the static posture training experiment. For the flexion trajectory, the two main degrees of freedom are the flexion of the lower segment and the flexion of the upper segment. For the compound trajectory, the main degrees of freedom were lateral bending and flexion of the end-effector. The coordination error for the flexion trajectory is calculated as follows:

$$\epsilon_f = \sqrt{(\phi_{lumbar,des} - \phi_{lumbar,act})^2 - (\phi_{thoracic,des} - \phi_{thoracic,act})^2}$$

The coordination error for the compound trajectory is calculated as:

$$\epsilon_c = \sqrt{(\phi_{ee,des} - \phi_{ee,act})^2 - (\theta_{ee,des} - \theta_{ee,act})^2}$$

Figure 3.8 shows the coordination error during the on-task phases of training and testing sessions. For the flexion trajectory, coordination error seemed roughly the same in both testing and training sessions, for both groups. The visual group had a slightly higher coordination error in both sessions. For the compound trajectory, the coordination error increased from testing to training for the force group, but remained about the same between sessions for the visual group. The visual group had slightly higher error during the training sessions, but comparable error during the testing sessions.

3.2.2 Discussion

The results suggest that while the group receiving force feedback was more quickly and reliably able to grasp the main concept of the trajectory, as shown by their lower amount of time spent in off-task movements during training. However, they consistently missed the finer points. For example in the flexion trajectory, they largely ignored the separation of lumbar and thoracic movement, and moved both segments together (but with the lumbar segment moving slightly faster). In the compound movement trajectory, they grasped that the trajectory involved moving the torso in a quarter-circle rotation, but added in a twisting motion during the testing phase. Since they did

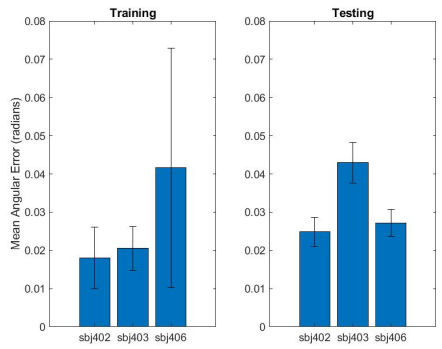

(a) Flexion Trajectory Mean Coordination Error, Force Group

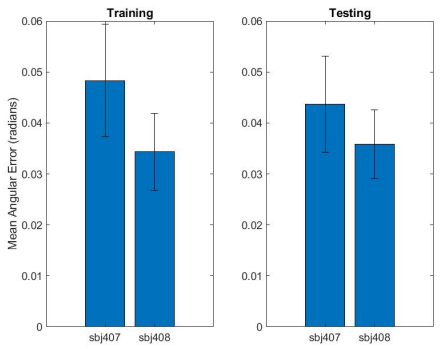

(b) Flexion Trajectory Coordination Angular Error, Visual Group

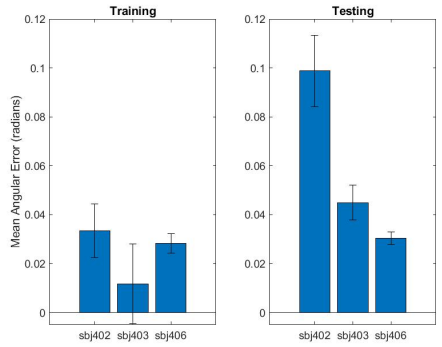

(c) Compound Trajectory Mean Coordination Error, Force Group

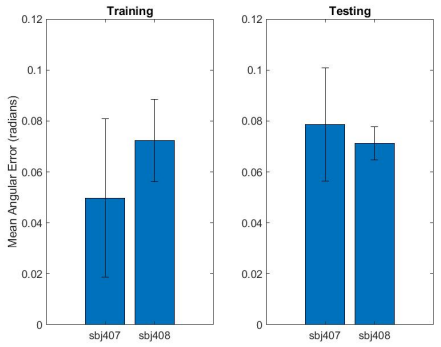

(d) Compound Trajectory Coordination Angular Error, Visual Group

Figure 3.8: Mean coordination error during the on-task phases of the trajectory for both groups.

not demonstrate that motion during training, it is possible that based their understanding of the trajectory on the expectation that a simultaneous twist was involved.

The group receiving visual feedback was less consistent in their performance. One subject was able to outperform the entire force feedback group while the other subject generally underperformed. The variable response suggests that visual feedback may encourage some individuals to achieve a higher level of success, but may be too difficult for others to interpret and learn effectively. While this study did not evaluate the effect of combining these feedback types, either sequentially or simultaneously, these results suggest that it might be a promising strategy. Combining feedback types may enable all users to reach the baseline level of success achieved in the force feedback group, and some individuals to achieve higher success through effective interpretation of

the visual feedback.

These results present an intriguing contrast to the results of the static posture learning experiment, in which the force feedback group consistently outperformed the visual feedback group. Since this task was simpler than the dynamic task, on possible explanation is that the force. One possible explanation is that this task was simpler than the dynamic task, such that there were no "nuances" for the force group to overlook. This further supports the idea that force feedback could be more useful for beginners attempting simple tasks, and visual feedback could be more useful for advanced users attempting more complex tasks.

3.3 Conclusion

In this section, we present the results of a novel training paradigm for torso motor learning of both static poses and dynamic movements. The key findings are that both torso motor learning paradigms, augmented visual and somatosensory feedback provided by the RoSE enabled users to learn static poses and movement trajectories. For static poses, force feedback was more effective, but for movement trajectories, visual feedback may be better for some users. These initial findings suggest that the RoSE may be able to provide users with additional types of sensory feedback that can aid in learning novel torso motor tasks, and suggest that it could be a useful tool for physical therapists treating scoliosis patients.

Chapter 4: Postural Assistance for Torso Motor Impairment

This chapter details the design of the wheelchair robot for active postural support (WRAPS). A 4 degree of freedom spatial parallel mechanism is employed to provide the user with trunk movement in the sagittal plane as well as lateral bending. The position and force control of the device are validated, and it is evaluated with a human user.

4.1 Design Requirement

The primary goal of the WRAPS design was to create a device that would aid those with trunk motor impairments in their activities of daily living. Some secondary considerations for this group are: to avoid postures which encourage the progression of scoliosis, to promote deep breathing, to distribute pressure evenly on the skin, and to keep the device low profile to be compatible with the wheelchair and to avoid social stigma.

Activities of daily living were determined through literature review and through user interviews. We interviewed three teenagers with cerebral palsy GMFCS level IV. All of these children wore a rigid TLSO and also used belts in their wheelchair. All three indicated that they wanted to be able to reach further forward and downward without fear of falling, such that they would be able to pet a dog. Other activities included getting things off a shelf independently and changing their resting position independently. We also interviewed an adult with a spinal cord injury, who expressed his wish to change his under-seat pressure distribution more easily and more often to prevent pressure sores.

The requested activities were translated into degrees-of-freedom using a motion capture (Vicon) experiment. During this experiment, a single subject would pick up an object from a shelf located in front at four different heights. For retrieving light objects, three degrees-of-freedom in

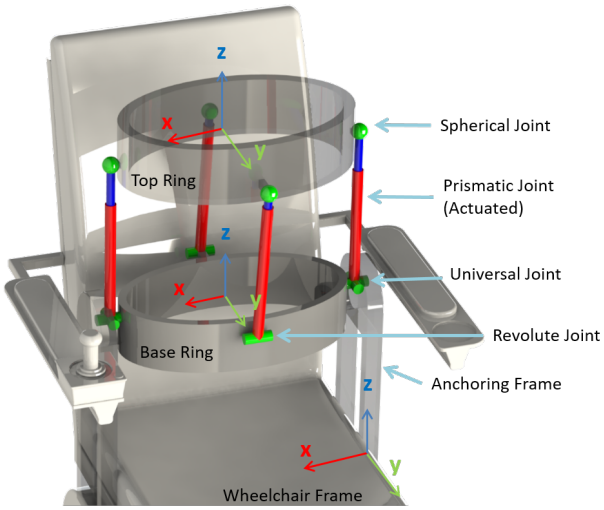

Figure 4.1: 2RPS-2UPS schematic

the sagittal plane were sufficient. For heavier objects, a small amount of lateral bending was also employed. Therefore, it was possible to achieve forward reaching tasks with a limited range of motion consisting of four degrees-of-freedom. While lateral bending tasks might be beneficial to some users, providing the lateral translation and axial rotation degree-of-freedoms would create a greater stability challenge, and could encourage a scoliotic posture, i.e., with twisting and leaning on one side. Limiting the degrees-of-freedom could also potentially make the device simpler and less obtrusive, leading to wider social acceptance.

The motion of the pelvis created another set of design requirements for the wheelchair mounting attachment. Even while sitting, the pelvis places an important role in functional activities. However, for people with trunk motor impairments, it is often a challenge to incorporate the pelvis into functional movements and maintain healthy alignment. Motor control of the trunk often starts at the neck and progresses down the trunk. For someone with incomplete trunk control, the lower segments of the trunk needs to be stabilized in order to effectively use the upper segments. Another consequence of trunk instability is that the pelvis can often end up habitually tilted in the frontal plane (pelvic obliquity) which can lead to functional and later structural scoliosis. It also concentrates the majority of the underseat pressure onto one ischial tuberosity, which puts one at risk for pressure sores. In addition, there is wide variation in the dimension and habitual posture

of the pelvis. In light of these restrictions, it is desirable to build an attachment mechanism that can accommodate a range of pelvis heights, widths, and anterior-posterior tilt angles, but which maintains a level pelvis in the frontal plane.

4.2 Proposed Design

The mechanism design, shown in Fig. 4.1, was chosen to achieve the desired degrees-of-freedom while meeting the unique needs of this group. The two ring design provides necessary support at the pelvis and thorax without restricting breathing from the belly. The two rings fit around the torso. The base ring shown (pelvic ring) rests just above the iliac crests of the wearer and the top ring shown (thoracic ring) would be at sternum level. To make the device low-profile, a parallel mechanism was preferred to a serial mechanism. The legs of the parallel mechanism can be placed around the body, while a serial chain could cause interference with the wheelchair.

The platforms are connected with two Rotational-Prismatic-Spherical (RPS) and two Universal-Prismatic-Spherical (UPS) kinematic chains to achieve the four desired DOF [52, 53]. The two RPS limbs are located in the sagittal plane, with the revolute (R) joints connected to the pelvic ring and the spherical (S) joints connected to the thoracic ring. The UPS limbs are located outside the sagittal plane, with the universal (U) joints connected to the pelvic ring and the S joints connecting to the thoracic ring. All four prismatic (P) joints are actuated. By orienting the axes of the R joints perpendicular to the sagittal plane, lateral translation and axial rotation are prevented. The end-effector has four remaining degrees-of-freedom and is fully actuated.

4.2.1 Joint Placement Optimization

The range of motion and the force capability of a parallel mechanism are very sensitive to the joint placement. Hence, an optimization was needed to maximize the force capability and the torso range of motion in the sagittal plane. To simplify the optimization routine, the spatial parallel mechanism can be seen as a planar 3-RPR mechanism in the sagittal plane as shown in Fig. 4.2, given that the universal joint positions are symmetrically placed along the sagittal plane. Note that

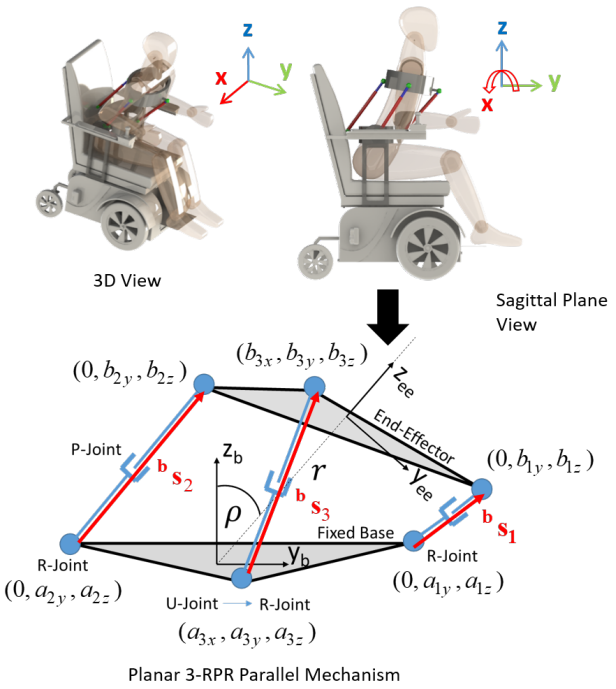

Figure 4.2: Model of a 2RPS-2UPS mechanism simplified to a 3-RPR mechanism in the sagittal plane

in this design, there are no singularities of the the rotation around the y-axis.

The torso was modeled as an inverted pendulum with the center of mass at the endpoint. The torso was assumed to bear all axial load from the weight. As the device is intended for use by individuals with torso motor impairments, it is expected that the dominant force on the WRAPS will be the weight of the user's torso, rather than user-generated force. In addition, given that the device is intended for those with substantial motor impairments, it is meant to provide slow, smooth movements rather than rapid, jerky ones, so a quasi-static analysis of the force is appropriate. The torso was modeled as an inverted pendulum with a pivot at the pelvis, shown in Fig. 4.4. The torso is considered a rigid link and is assumed to bear all of the axial load from its weight. It was assigned a mass of 50 kg and a COM height of 0.25 m, following ISO 7176-11 standard for a 75 kg wheelchair rider.The maximum bending degree was determined to be approximately 1 radian [54].

The optimization is based on the Generalized Pattern Search Algorithm (GPSA) [55]. The

algorithm is implemented with the Matlab Genetic Algorithm and Direct Search Toolbox [56].

Fig. 4.2 shows the 12 parameters to be optimized: $(a_{iy}, a_{iz}, b_{iy}, b_{iz},\ i = 1, 2, 3)$, which are the R, U, and S joint locations in the sagittal plane. In this case, $a_{1x} = a_{2x} = b_{1x} = b_{2x} = 0$ because the anterior and posterior limbs are in the sagittal plane and a_{3x}, b_{3x} are constant because of the width of the torso. Further constraints resulting from the length and stroke of candidate linear actuators are shown in Tab. 4.1.

First, we normalized these parameters to the same scale. For example, $a_{1y} \in [a_{1y}^{min}, a_{1y}^{max}]$ is converted to $\eta_1 \in [0, 12]$. The acceptable ranges for these parameters are based on the dimensions of the torso and the acceptable amount of offset from the body. They are shown in Tab. 4.2. Then, all 12 normalized parameters η_i are used to calculate a fitness value of a set of input parameters. The fitness function $F(\eta)$ is evaluated in the following steps:

1. The algorithm samples a configuration of the end-effector in the polar coordinate in the sagittal plane (ρ, r) approximating the forward/backward bending motion of the torso. The parameters of the workspace sample are given in Tab. 4.1.

2. The vectors of three limb lengths are calculated based on the current end-effector orientation with respect to the base frame, namely

$$ {}^{\mathbf{b}}\mathbf{s}_i = \begin{bmatrix} s_{ix} \\ s_{iy} \\ s_{iz} \end{bmatrix} = \begin{bmatrix} b_{ix} - a_{ix} \\ -a_{iy} + b_{iy}\cos\rho + (b_{iz} + r)\sin\rho \\ -a_{iz} + (b_{iz} + r)\cos\rho - b_{iy}\sin\rho \end{bmatrix} \tag{4.1} $$

3. The dimensionally homogeneous Jacobian, $\tilde{J}$, modified from the Jacobian mapping between the joint forces to the end-effector wrench of the equivalent 3-RPR mechanism in the sagittal plane, is calculated as follows [57, 58]

$$ \tilde{J} = \begin{bmatrix} {}^{\mathbf{b}}\mathbf{w_1} & {}^{\mathbf{b}}\mathbf{w_2} & {}^{\mathbf{b}}\mathbf{w_3} \end{bmatrix}_{3\times 3} \tag{4.2} $$

where

$${}^{\mathbf{b}}\mathbf{w_i} = \begin{bmatrix} \frac{1}{L}w_{ix} \\ \hat{s}_{iy} \\ \hat{s}_{iz} \end{bmatrix}, L = \sqrt{\frac{1}{3}\sum_{i=1}^{3}|w_{ix}|^2} \text{ (characteristic length)}$$

$$w_{ix} = (b_{iy}\cos\rho - b_{iz}\cos\rho)\hat{s}_{iy} - (b_{iy}\sin\rho + b_{iz}\cos\rho)\hat{s}_{iz},$$

$$\hat{s}_{iy} = \frac{s_{iy}}{\sqrt{s_{iy}^2+s_{iz}^2}}, \text{ and } \hat{s}_{iz} = \frac{s_{iz}}{\sqrt{s_{iy}^2+s_{iz}^2}}$$

4. Each sampled point is tested by two conditions. First, all required limb lengths must be feasible. The allowable range on each limb is determined by the stroke length of the linear actuator and dimensions in CAD. The condition is

$$\left\|{}^{\mathbf{b}}\mathbf{s_i}\right\| \in \left[{s_i}^{\min}, {s_i}^{\max}\right], i = 1, 2, 3 \tag{4.3}$$

The second condition is that the condition number of the Jacobian $\tilde{J}$ is less than a specific value to avoid singularities, namely

$$\kappa(\tilde{J}) = \frac{\sigma_{\max}(\tilde{J})}{\sigma_{\min}(\tilde{J})} < \kappa_{max} \tag{4.4}$$

where $\sigma_{\max}(\tilde{J})$ and $\sigma_{\min}(\tilde{J})$ are maximal and minimal singular values of the matrix $\tilde{J}$, respectively. If both of the conditions in Eqn. (4.3) and (4.4) are met, the current sampled point will be marked as feasible.

5. Once the algorithm has gone through all points in the workspace, the fitness function output is

$$F(\eta) = 1 - \frac{N_{feasible}}{N_{sample}}, \tag{4.5}$$

Table 4.1: Optimization parameters

Workspace		Constraints	
r	[0.275, 0.325] m	$\left\|{}^{\mathbf{b}}\mathbf{s_1}\right\|$	[0.332, 0.472] m
Δr	0.0020833 m	$\left\|{}^{\mathbf{b}}\mathbf{s_2}\right\|$	[0.332, 0.472] m
ρ	[-0.2, 0.7] rad	$\left\|{}^{\mathbf{b}}\mathbf{s_3}\right\|$	[0.244, 0.344] m
$\Delta\rho$	0.025 rad	κ_{max}	8
N_{sample}	925	a_{3x}, b_{3x}	0.2 m

Table 4.2: Optimization results of joint positions

Base Ring	Range (m)	Initial Guess (m)	Optimized (m)
a_{1y}	[0.135, 0.2]	0.15	0.1351
a_{1z}	[-0.055, 0.055]	-0.025	-0.0549
a_{2y}	[-0.225, -0.185]	-0.185	-0.185
a_{2z}	[-0.055, 0.1]	0	-0.0198
a_{3y}	[-0.15, 0.1]	0.1	0.1
a_{3z}	[-0.055, 0.055]	0	0.0092
Top Ring	Range (m)	Initial Guess (m)	Optimized (m)
b_{1y}	[0.115, 0.175]	0.175	0.175
b_{1z}	[-0.055, 0.055]	0	0.055
b_{2y}	[-0.175, 0.130]	-0.175	-0.145
b_{2z}	[-0.1, 0.055]	0	0.0517
b_{3y}	[-0.1, 0.1]	-0.05	-0.05
b_{3z}	[-0.055, 0.055]	-0.05	-0.0317

where $N_{feasible}$ and N_{sample} are the number of all feasible points in the workspace and the total number of points in sampled workspace respectively.

The optimization results are shown in Tab. 4.2 and illustrated in Fig. 4.3. The initial set of joint position parameters in Fig. 4.3 (A) provides only a small number of feasible points in the sampled workspace, enclosed by dotted lines. The GPSA algorithm outputs an optimized set of joint positions in Fig. 4.3 (B) with a significantly higher number of feasible points.

4.2.2 Joint Force Requirements

After the joint positions had been optimized to provide the desired workspace, the required joint forces were determined. In the most extreme flexion position, the forces in the prismatic

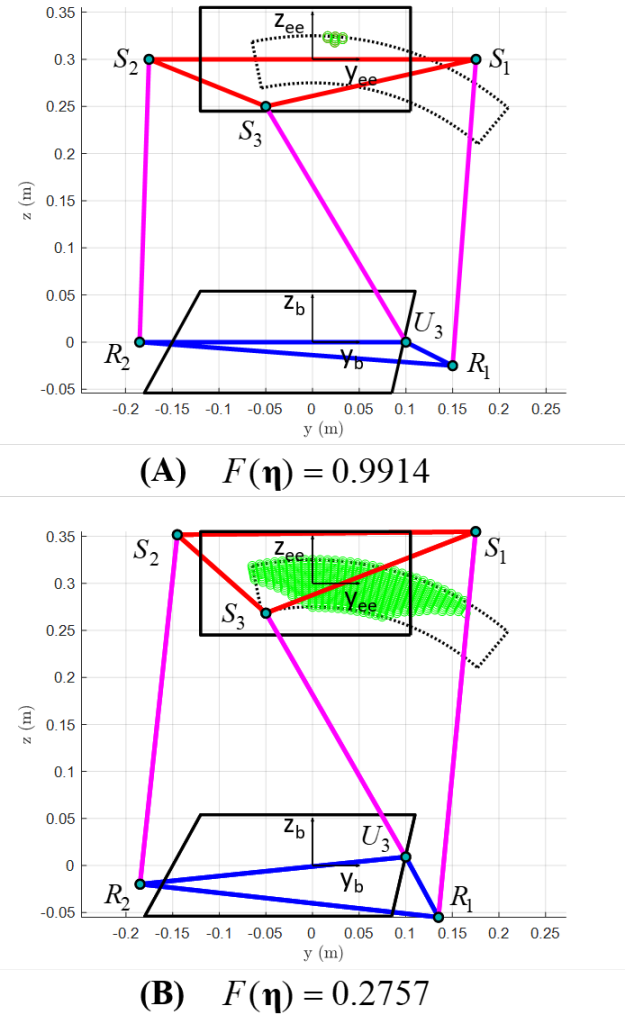

Figure 4.3: Comparison between the fitness function values of the initial set of parameter (A) and the final solution (B)

joints are 133.95 N on the front limb (RPS1), 253.82 N on the back limb (RPS2), and 230.81 N in the two side limbs (UPS). The gear ratio of the linear actuators were selected based on this specification. Joint forces were measured in real time through load cells placed in series with the actuator in each limb.

4.3 Mathematical Model

The kinematic diagram of the 2RPS-2UPS parallel mechanism is shown in Fig. 4.5. The line formed by the centers of the two revolute joints (R_1 and R_2) and the origin of the fixed base

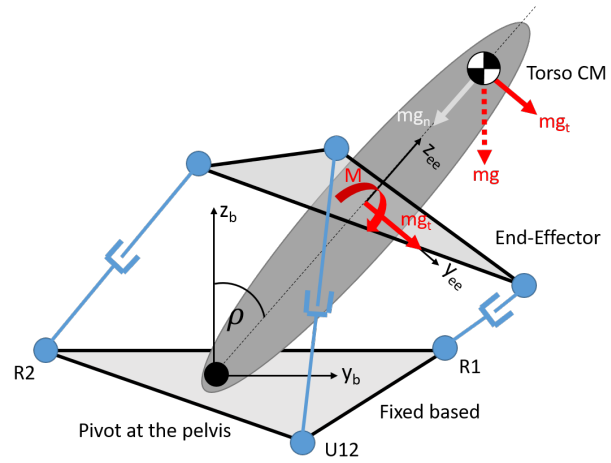

Figure 4.4: Forces applied to WRAPS by the torso weight

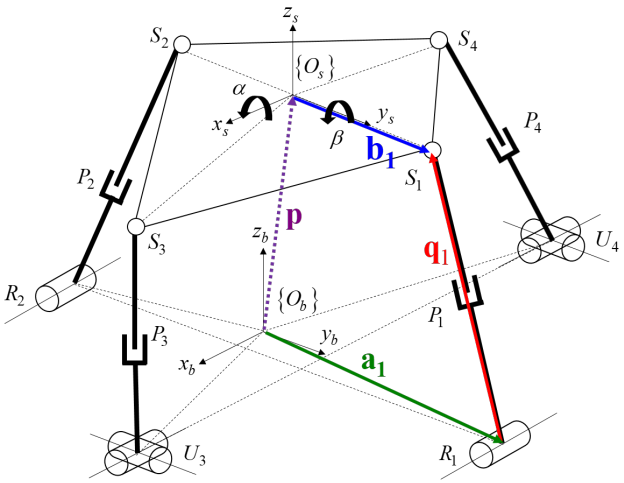

Figure 4.5: Kinematic diagram of a 2RPS-2UPS parallel actuated platform

coordinate frame $\{O_b\}$ is selected to be the sagittal plane (y_b-z_b plane). The origin of a coordinate frame $\{O_s\}$ on the end-effector is inside the line connecting the centers of the two spherical joints (S_1 and S_2) of the two RPS limbs. Since the revolute joints constrain the line S_1S_2 in the sagittal plane, the y_s axis that is parallel to this line is also kept in the the sagittal plane. $\mathbf{a_i}$ are the vectors of joint positions with respect to the base frame, while $\mathbf{b_i}$ are the vectors of the spherical joint positions with respect to the local frame $\{O_s\}$.

4.3.1 Inverse Kinematics

A configuration of the robot is determined by a set of four variables (y, z, α, β). The variables y and z are the origin position of the end-effector frame $\{O_s\}$ relative to the origin of the base frame $\{O_b\}$ and α and β are the Euler angles in the current X-Y sequence.

Given the position and orientation of the end-effector frame $\{O_s\}$ relative to the base frame $\{O_b\}$, we have to find the required four limb lengths to achieve this configuration. The commanded position and orientation from the four input variables (y, z, α, β) can be transformed into all four limb lengths $\mathbf{q_i} = [q_1, q_2, q_3, q_4]^T$ by using the close-loop kinematic constraints as shown in Fig. 4.5

$$\begin{aligned} \mathbf{q_i} &= \mathbf{p} + R\mathbf{b_i} - \mathbf{a_i} \quad (i = 1, 2, 3, 4) \\ q_i &= \|\mathbf{q_i}\| = \left[(\mathbf{p} + R\mathbf{b_i} - \mathbf{a_i})^T(\mathbf{p} + R\mathbf{b_i} - \mathbf{a_i})\right]^{1/2} \end{aligned} \tag{4.6}$$

where $\mathbf{p} = [0, y, z]^T$, and $R = \begin{bmatrix} c\beta & 0 & s\beta \\ s\alpha s\beta & c\alpha & -s\alpha c\beta \\ -c\alpha s\beta & s\alpha & c\alpha c\beta \end{bmatrix}$

$s\theta$ and $c\theta$ are the short-hand notations for $\sin\theta$ and $\cos\theta$.

4.3.2 Forward Kinematics

An analytical solution to the forward kinematics has been found for a special case of this 2RPS-2UPS structure in which the joints on each platform lie in the same plane [53]. Thus, we use the Newton-Raphson algorithm to calculate the iterative solution from a given set of limb lengths [59]. The Newton-Raphson formula in the vector form is

$$\mathbf{X_{n+1}} = \mathbf{X_n} + J_f^{-1}(\mathbf{X_n})\mathbf{d_n} \tag{4.7}$$

where $\mathbf{X} = \begin{bmatrix} x & y & \alpha & \beta \end{bmatrix}^T$, and subscript n denotes the solution at iteration step n, and $\mathbf{d_n}$ is a vector consisting of $d_{ni} = -f_i(\mathbf{X_n}),\ i = 1, 2, 3, 4$. The scalar function f_i is derived from Eqn. (4.6)

to be

$$f_i(\mathbf{X}) = (\mathbf{p} + R\mathbf{b_i} - \mathbf{a_i})^T(\mathbf{p} + R\mathbf{b_i} - \mathbf{a_i}) - {q_i}^2 = 0 \tag{4.8}$$

The algorithm is performed by the following steps.

1. At step n, specify an initial guess $\mathbf{X_n}$.

2. Compute the iterative Jacobian $J_f(\mathbf{X_n})$.

3. Compute the vector of scalar functions $\mathbf{d_n}$.

   If $\sum_{i=1}^{4} |d_{ni}| < \varepsilon_b$ (a specified tolerance for the sum of vector components), stop and use $\mathbf{X_n}$ as the solution.

4. Solve for the incremental vector $\delta\mathbf{X_n}$ from $J_f\delta\mathbf{X_n} = \mathbf{d_n}$.

   If $\left\|\delta\mathbf{X_{c,n}}\right\| < \varepsilon_x$ (a specified tolerance for the size of incremental vectors), stop and use $\mathbf{X_n}$ as the solution.

5. Update $\mathbf{X_{n+1}} = \mathbf{X_n} + \delta\mathbf{X_n}$, and repeat the first step if $n < n_{\max}$ (maximum number of iteration steps).

The solution obtained at iteration step n is used as the initial guess in the next time step, when we obtain a new set of limb lengths q_i, to reduce the computational time and obtain continuous solutions. The very first time step uses the neutral configuration as the initial guess.

4.3.3 Kinematics of an Arbitrary End-Effector Frame

In Sections 4.3.1 and 4.3.2, we used an end-effector coordinate frame $\{O_s\}$ that is properly aligned within the robot architecture such that position and orientation of the frame in 3D space can be described by exactly four independent variables (y, z, α, β). However, in real implementations, the prescribed end-effector frame $\{O_{ee}\}$, which is the position of the upper trunk from the optimization in Section 4.2.1, has an arbitrary offset of both position and orientation from the

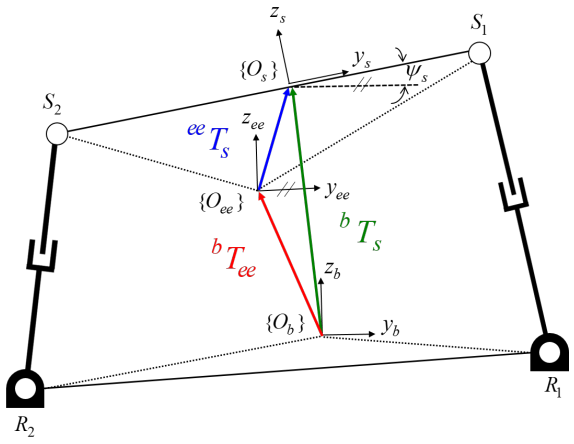

Figure 4.6: Transformations between coordinate frames in sagittal plane

frame $\{O_s\}$ in the local y_s-z_s plane. Nevertheless, we can employ homogeneous transformation matrices to find the position and orientation of the actual end-effector frame in terms of the four variables (y, z, α, β) obtained from the forward kinematics solution, as shown in Fig. 4.6.

4.3.4 Output Force and Moment

The forces and moments in six degrees-of-freedom $\mathbf{F}$ at the origin of the end-effector with respect to the base frame can be calculated from the vector of joint forces τ as follows

$$\mathbf{F} = J_s^{\,T}\tau \tag{4.9}$$

where J_s is the screw-based velocity Jacobian, derived by taking the orthogonal product of each selected reciprocal screw and the instantaneous twist of its respective limb. The selected reciprocal screw is reciprocal to all passive joint screws in the instantaneous twist equation, except for its respective actuated joint screw [60]. For a 2RPS-2UPS mechanism, the Jacobian is in the following

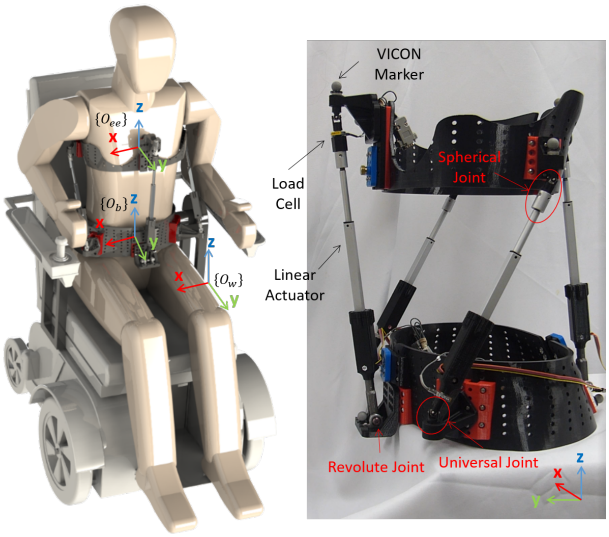

Figure 4.7: CAD design of WRAPS mounted on wheelchair and the real prototype

form [53]

$$J_s = \begin{bmatrix} \hat{\mathbf{q}}_1^T & (R\mathbf{b_1} \times \hat{\mathbf{q}}_1)^T \\ \vdots & \vdots \\ \hat{\mathbf{q}}_4^T & (R\mathbf{b_4} \times \hat{\mathbf{q}}_4)^T \\ \hat{\mathbf{x}}^T & (R\mathbf{b_1} \times \hat{\mathbf{x}})^T \\ \hat{\mathbf{x}}^T & (R\mathbf{b_2} \times \hat{\mathbf{x}})^T \end{bmatrix}_{6\times 6}, \ \hat{\mathbf{x}} = [1,0,0]^T$$

From the Jacobian, one can easily observe that the forces and the moments in the sagittal plane (f_y, f_z, m_x) are fully determined by the forces measured from the four load cells along the limbs, while the other components of forces and moments need to be calculated from the unmeasured constraint forces along the revolute joint axes. Hence, the force measurement will be collected only in the sagittal plane components, and the dimension of the Jacobian transpose ${J_s}^T$ can be reduced to 3×4.

4.4 Hardware Realization

A first prototype of the device has been created for evaluation, as shown in Fig. 4.7. The two rings were designed from a body scan of a healthy adult male and were made of 3D-printed ABS

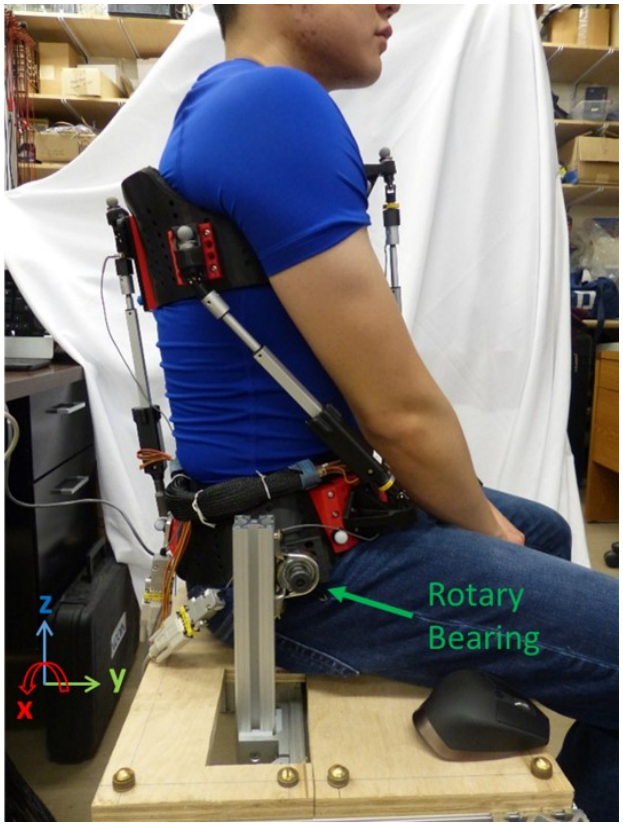

Figure 4.8: Subject wearing the WRAPS

plastic (Stratasys, Fortus 360 mc). The rings have adjustable width and are lined with a soft foam padding (Rolyan, Polycushion Padding) to distribute pressure and improve wearer comfort. The device is actuated by Actuonix Micro-linear actuators (L16-100-150-12-P in the UPS limbs and L16-140-150-12-P in the RPS limbs). The motors have a 100 mm and 140 mm stroke, respectively, and their maximum force is 250 N. They are driven at 12 V using a 1000 Hz PWM signal through a small driver (Toshiba, TB6612FNG). These motors contain an on-board potentiometer, and are placed in series with a load cell (FUTEK, LCM 200 Miniature Tension and Compression Load Cell with IAA100 Analog Amplifier with Voltage Output). The signals from these sensors are multiplexed and sent to a portable reconfigurable I/O (RIO) device (National Instruments, myRIO-1900) as a control board. The pelvic ring can be attached to a custom-made bench by two bearings which accommodate passive range of motion from the pelvic tilt while seated, as shown in Fig. 4.8. Alternatively, this joint can be fixed at any angle, to prevent the pelvis from rotating. The position

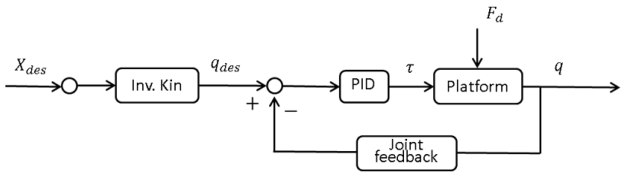

Figure 4.9: Position control mode

of these bearings can be adjusted to accommodate individuals of different height and width of pelvis.

4.5 Evaluation

The performance of the device has been evaluated against reference systems in terms of the accuracy of the forward kinematics algorithm, the force-moment output calculated from the forces along the limbs, and the capability to support the torso.

4.5.1 Forward Kinematics Validation

The forward kinematics of the device was validated using a motion-capture camera system (Bonita, Vicon Motion Systems, Oxford, UK). The robot configuration is controlled in the position mode as shown in Fig. 4.9. The actual position and orientation of the end-effector is calculated using the four variables (y, z, α, β) obtained from solutions of forward kinematics according to Sections 4.3.2 and 4.3.3.

The accuracy of the forward kinematics is shown in Figs. 4.10 and 4.10. In Fig. 4.10, the device was commanded to rotate about the x-axis and move forward and down in a flexion/extension motion. The mean absolute error (MAE) of rotation about the x-axis, which was the primary direction of motion, was 1.08 degrees. The maximum MAE was 3.80 mm in the z direction, and the maximum MAE error in rotation was 3.28 degrees about y.

In Fig. 4.11, the device moved in a complex motion that combined all four degrees-of-freedom. The maximum RMS translational error was 3.96 in the z direction and the maximum RMS rotational error was 2.55 degrees about y. For all directions, the translational error was within 4 mm

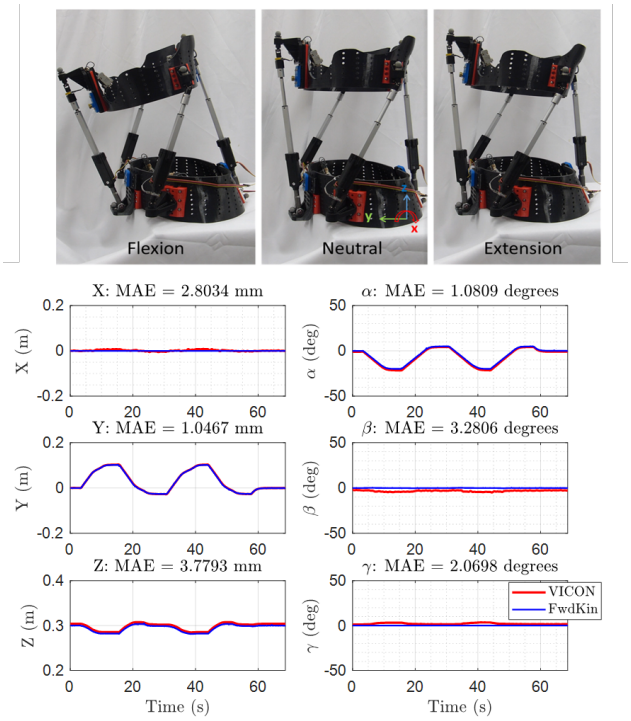

Figure 4.10: Flexion-Extension motion (rotation about x, with translation in y and z)

and the rotational error was within 3 degrees. The degrees-of-freedom with the largest errors were translation in z and the rotation about y. The error is due in part to manufacturing, including motion from imprecise joint tolerance and an initial angular offset between the rings. The initial offset of the top ring relative to the pelvis ring is not zero in some degrees-of-freedom, which causes the position measured from the motion capture system to show the initial offset error relative to the forward kinematic solution. Nevertheless, the predominant errors are from these initial offsets, and the problem can be easily fixed in the hardware.

4.5.2 Output Force and Moment Validation

The output wrench in the sagittal plane was evaluated. The pelvis ring was fixed to the bench and the thorax ring was attached to an ATI Mini45 Force/Torque Sensor, which was fixed to the frame, Fig. 4.12. The robot was controlled in force mode as shown in Fig. 4.13. Forces in the y- and z-direction, as well as a moment about x were, simultaneously applied with a frequency of 0.25 Hz and amplitude of 2 N, 5 N, and 2.5 N-m, respectively, as shown in Fig. 4.14. The root

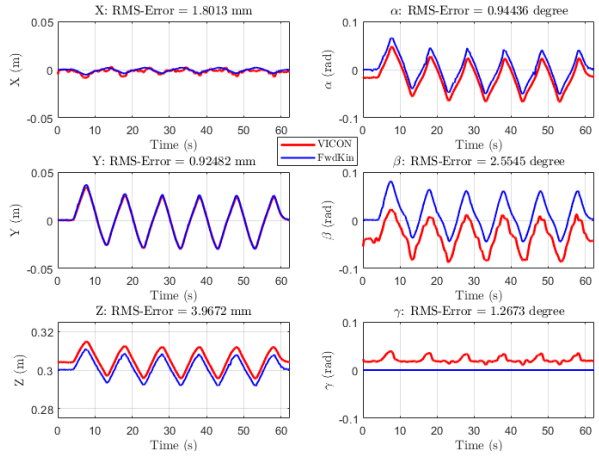

Figure 4.11: Compound Out-of-Plane Movement (y-z translation and rotation about x and y)

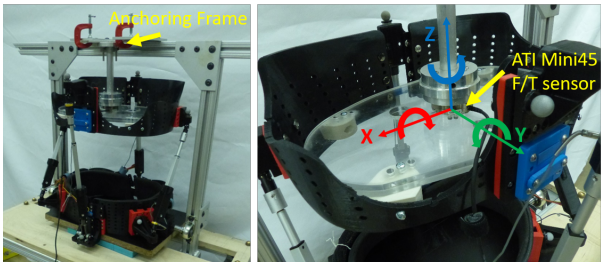

Figure 4.12: Test rig for the force-torque output validation

mean square (RMS) of the error in the y- and z-directions were 0.866 N and 1.312 N respectively. The RMS of the error in the moment about x was 0.279 N.

4.5.3 Human Evaluation

An experiment was conducted to determine the user's range of motion (ROM) in the brace and to validate the brace's ability to support the torso throughout the ROM. This experiment was approved by the Institutional Review Board of Columbia University (Protocol AAAP7105). The subject was a 183 cm, 79 kg, 25 year old male without neuromotor impairment. He wore the brace while seated on on the bench. The subject's hip position and orientation were fixed with the bench attachment and the motion of the thoracic ring relative to the pelvis ring was assessed.

First, the ROM of a subject was assessed in transparent (zero-force control) mode. The subject was able to achieve a range of $+10°$ to $-10°$ in flexion/extension, and $+5°$ to $-6°$ in lateral bending.

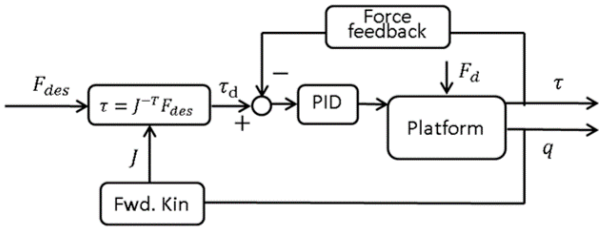

Figure 4.13: Force control mode

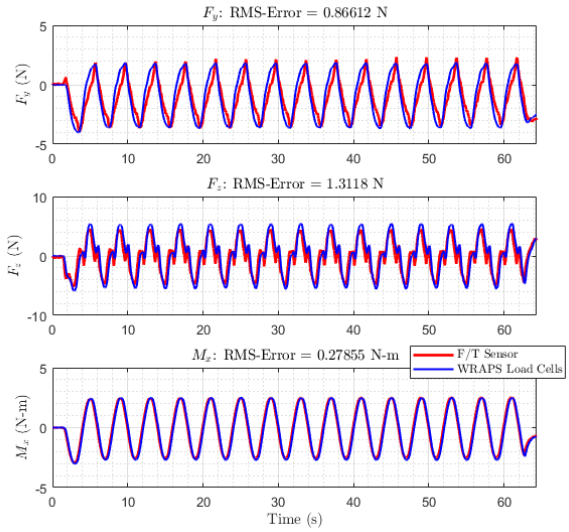

Figure 4.14: Force-moment accuracy

The subject was then moved through their range of motion in assistive (position control) mode. For this session, the brace copied the trajectories generated by the subject in the previous session (transparent mode). The subject was instructed to remain passive and allow the brace to move them. The WRAPS was able to support the torso throughout the ROM, sustaining up to 40 N of force and 10 N-m of moment, as shown in Fig. 4.15.

4.6 Future Work

Future work includes further improving the ergonomic design of the device as well as evaluating its effectiveness in assisting human subjects. Currently, limb attachment points have been optimized based on the range of motion of the device in the sagittal plane. The design could potentially be improved by also optimizing for the range of motion in rotation about the y axis. Also,

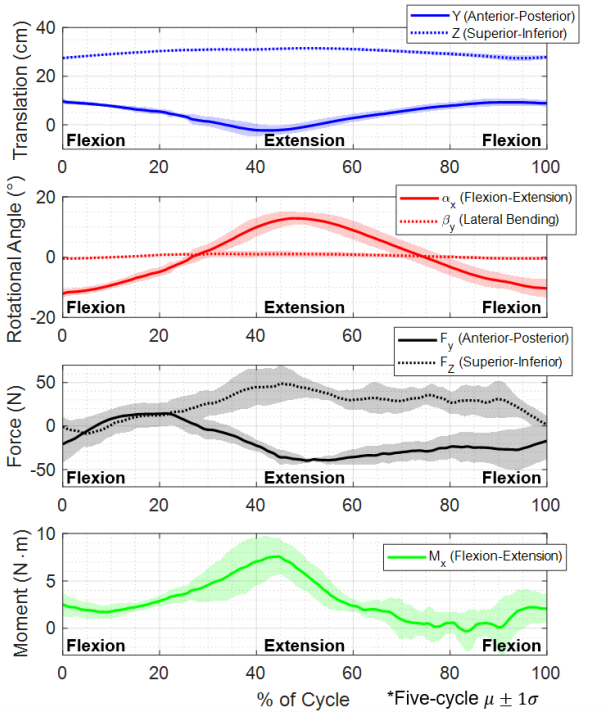

Figure 4.15: Kinematics and Forces of Flexion/Extension in Assistive Mode

the anthropometric data can be collected by a motion capture system. The pelvis ring attachment could be improved. An active pelvis device may improve the range of center of pressure excursion. In addition, it could make the reaching trajectory more natural.

In addition, the device needs to be evaluated in human subjects to determine the best control paradigm for assisting users. While the WRAPS has position and force control modes, the best interface for users remains to be seen. Individuals with trunk motor impairments often have other neuromuscular impairments or cognitive impairments that may make operating the device more challenging. Developing a reliable method of detecting user intent in these circumstances could improve the device.

4.7 Conclusions

This chapter proposes a novel active postural support with strong potential to aid individuals with trunk motor control impairments. The device is a parallel mechanism consisting of two RPS

limbs in the sagittal plane, and two UPS limbs outside of the plane. The design was motivated by the limitations imposed by static supports that are currently used to promote healthy posture in this population, but that are overly restrictive. The WRAPS was designed to help users achieve a range of functional tasks without fear of falling and to encourage healthy posture.

Conclusion

The key contributions of this work are two robotic torso exoskeletons, as well as a first characterization of the torso stiffness of female adolescents with and without scoliosis, and first application of robotic exoskeleton to augmented sensory feedback for direct posture learning tasks. The first exoskeleton adapts an existing design to meet the needs of the Adolescent Idiopathic Scoliosis population, and to conduct these studies on torso stiffness and posture learning. The other exoskeleton proposes a novel design to assist wheelchair users with torso motor impairments, while restricting them from postures associated with the development neuromuscular scoliosis.

Translational Design

In my adaptation of the RoSE design, I was able to meet the needs of the AIS clinical population by creating a smaller and lighter exoskeleton able to accomodate a range of torso sizes. This brace design enable me to pursue novel research questions with this population, and will enable future researchers to work with this population in the future. Likewise, in the WRAPS design, I proposed a design that would meet the needs of the neuromuscular scoliosis population by balancing the competing demands of functional movement and posture support. This device is the first to offer active posture support to help users achieve tasks of daily living, while simultaneously preventing postures associated with neuromuscular scoliosis progression.

New knowledge on the torso stiffness of female adolescents

For the first time in the literature, I compared the three-dimensional stiffness characterization for female adolescents with and without scoliosis. The key findings include an interaction effect of DOF and torso segment on translational collinear stiffnesses, and an interaction effect of DOF and group on rotational collinear stiffnesses. In addition, the data provided could be used to create a more accurate finite element models of the torso, which could improve scoliosis orthotics. The RoSE itself and the methodology presented here could also be used to obtain personalized stiffness characteristics for individuals with scoliosis, and perhaps lead to individualized FEM models, and more precise bracing outcomes.

New approaches to direct posture learning

I use the RoSE device to provide sensory feedback for motor learning tasks. This was inspired by the demands of scoliosis specific physical therapy. I found that while force feedback produced better results for static postures, for dynamic postural movements, the results are more complex. In these tasks, force feedback can result in quicker learning of the basic trajectory shape, but visual feedback may help users grasp the nuances of the movement.

Future Directions

The robotic devices and experimental methodologies can provide tools for further research in the field. For the RoSE, further study of those with AIS could help to elucidate the effect of additional variables on torso stiffness, such as curve magnitude and skeletal maturity. It could also be used to mimic the effect of various braces on an individual. For example, a three-dimensional scan of their current orthoses could be segmented into cross-sections. The RoSE could mimic this braces by copying the position and orientation of three cross-sections from their orthosis. The patient could then don the RoSE, and it could quantify the forces and moments applied to the body. Another extremely promising area would be to use the RoSE in combination with low-dose

radiography, such as the EOS system. This system can provide a three-dimensional representation of the spine with a fraction of the radiation used in a standard chest x-ray [61]. It could used on an individual basis, to find the relative position and orientation of three cross-sections of the torso that result in the greatest correction of the spine, and this information could form the basis of a patient-specific rigid orthosis design. Alternatively, it could be used with a methodology similar to chapter 2 to quantify the displacement of the spine as a function of the forces applied to the torso. This information would be even more useful for the development of representative FEM models of the adolescent torso and spine.

In terms of motor learning, the studies presented in chapter 3 raise several further questions. In the future, it would be interesting to further test the effects of combined sensory feedback. One way would be to allow subjects to train with first one type of feedback and then the other, and assess the effect of feedback order on their performance, and also compare to a group receiving both types of feedback simultaneously. In addition, it would be intriguing to compare these results to more traditional learning tools, such as verbal instruction, personal demonstration, and mirror use. While identifying the correct posture is the initial challenge in AIS physical therapy, learning to replicate it consistently, and eventually, unconsciously, is the end goal. The studies presented in chapter 3 did not look at long-term retention of the motor learning, but future studies should examine how well subjects are able to retain their learning, as well as the best strategies for weaning off the augmented sensory feedback to achieve this goal.

Another crucial area of future work is translating this learning paradigm to the adolescents with scoliosis. The results of this study suggests that the RoSE could be a powerful tool in the physical therapist's toolbox, but in order to be useful the methodology needs to be adapted to the clinical population and proven effective in that group. First, one needs to replicate this study with individuals with AIS, to verify that the individuals with scoliosis respond to sensory feedback in the same way as unaffected individuals. Then, a methodology must be developed to generate motor learning protocols specific to the individual's spine.

Finally, there are several promising directions available for the WRAPS. Since its initial design, it

has been evaluated in a wider group of human subjects, and shown to support users in their torso range of motion while reducing the muscle activation in their torso[62]. A 3 degree of freedom, fully active parallel mechanism has been designed that can be used in conjunction with the WRAPS to assist with seated pelvis range of motion [63]. This may enhance the range of functional movements the user can perform. Another important task in order to translate this work to the clinical population will be to develop an intuitive user interface for the device. Many people with torso neuromotor impairments also have impaired motor function in the limbs, so developing a reliable method of interpreting user intent presents an important challenge.

Taken together, these results illustrate the potential of robotic exoskeletons as tools for torso study, training, and assistance, and provide a foundation for further development of novel devices for scoliosis research and treatment. It is hoped that the exoskeleton designs and the studies presented here will be further the fields of scoliosis and trunk neuromotor impairment research, and will contribute to enhanced health and function of the torso-spine system for many people in the future.

References

[1] M. R. Konieczny, H. Senyurt, and R. Krauspe, "Epidemiology of adolescent idiopathic scoliosis," *Journal of Children's Orthopaedics*, vol. 7, p. 3, 1 Feb. 2013.

[2] S. L. Weinstein, L. A. Dolan, J. G. Wright, and M. B. Dobbs, "Effects of bracing in adolescents with idiopathic scoliosis," *New England Journal of Medicine*, vol. 369, pp. 1512–1521, 16 Oct. 17, 2013.

[3] C. Delphia, *Scoliosis in children and adolescents*, 2017.

[4] A. Jalalian, I. Gibson, and E. H. Tay, "Computational biomechanical modeling of scoliotic spine: Challenges and opportunities," *Spine Deformity*, vol. 1, pp. 401–411, 6 Nov. 1, 2013.

[5] A. Jalalian, F. E. H. Tay, S. Arastehfar, and G. Liu, "A new method to approximate load-displacement relationships of spinal motion segments for patient-specific multi-body models of scoliotic spine," *Medical & Biological Engineering & Computing*, vol. 55, pp. 1039–1050, 6 Jun. 1, 2017.

[6] J. P. Little and C. Adam, "Patient-specific computational biomechanics for simulating adolescent scoliosis surgery: Predicted vs clinical correction for a preliminary series of six patients," *International Journal for Numerical Methods in Biomedical Engineering*, vol. 27, pp. 347–356, 3 2011.

[7] S. P. S. B. I. T. N. Cobetto C. E. Aubin and H. Labelle, "3D correction of AIS in braces designed using CAD/CAM and FEM: A randomized controlled trial," *Scoliosis Spinal Discord*, vol. 12, no. 24, 2017.

[8] S. Bidari, M. Kamyab, H. Ghandhari, and A. Komeili, "Efficacy of computer-aided design and manufacturing versus computer-aided design and finite element modeling technologies in brace management of idiopathic scoliosis: A narrative review," *Asian Spine Journal*, vol. 15, p. 271, 2 Apr. 2021.

[9] C. Coillard, V. Vachon, A. B. Circo, M. Beauséjour, and C. H. Rivard, "Effectiveness of the SpineCor brace based on the new standardized criteria proposed by the scoliosis research society for adolescent idiopathic scoliosis," *Journal of Pediatric Orthopaedics*, vol. 27, pp. 375–379, 4 Jun. 2007.

[10] T. B. Grivas, A. Bountis, I. Vrasami, and N. V. Bardakos, "Brace technology thematic series: The dynamic derotation brace," *Scoliosis*, vol. 5, p. 20, Sep. 21, 2010.

[11] N. Nakamura, M. Uesugi, Y. Inaba, J. Machida, S. Okuzumi, and T. Saito, "Use of dynamic spinal brace in the management of neuromuscular scoliosis: A preliminary report," *Journal of Pediatric Orthopaedics*, vol. 23, pp. 291–298, 3 2003.

[12] J. P. A. Nijssen, G. Radaelli, J. L. Herder, C. J. Kim, and J. B. Ring, "Design and analysis of a shell mechanism based two-fold force controlled scoliosis brace," in *ASME 2017 International Design Engineering Technical Conferences and Computers and Information in Engineering Conference*, Cleveland, OH, Nov. 3, 2017.

[13] S. D. Voinier, "Passive stiffness characteristics of the scoliotic lumbar torso in trunk flexion, extension, lateral bending, and axial rotation," M.S. thesis, Virginia Polytechnic Institute, 2015.

[14] J. Park, P. R. Stegall, D. P. Roye, and S. K. Agrawal, "Robotic spine exoskeleton (RoSE): Characterizing the 3-d stiffness of the human torso in the treatment of spine deformity," *IEEE Transactions on Neural Systems and Rehabilitation Engineering*, vol. 26, pp. 1026–1035, 5 May 2018.

[15] N. Karavidas, "Bracing in the treatment of adolescent idiopathic scoliosis: Evidence to date," *Adolesc Health Med Ther*, vol. 10, pp. 153–172,

[16] H. Berdishevsky *et al.*, "Physiotherapy scoliosis-specific exercises – a comprehensive review of seven major schools," *Scoliosis and Spinal Disorders*, vol. 11, 1 Aug. 2016.

[17] L. Marin *et al.*, "Acute effects of self-correction on spine deviation and balance in adolescent girls with idiopathic scoliosis," *Sensors*, vol. 22, 5 Mar. 2022.

[18] M.-A. Giordamni, K. Chandolias, D. Pollatos, A. Chalkia, and E. Trevlaki, "Adolescent idiopathic scoliosis: Review of conservative treatment with physiotherapy scoliosis specific exercises," *International Journal of Health Sciences and Research (www.ijhsr.org)*, vol. 11, p. 88, 2021.

[19] I. Hatzilazaridis, V. Hatzitaki, N. Antoniadou, and E. Samoladas, "Postural and muscle responses to galvanic vestibular stimulation reveal a vestibular deficit in adolescents with idiopathic scoliosis," *European Journal of Neuroscience*, vol. 50, pp. 3614–3626, 10 Nov. 2019.

[20] J. P. Pialasse, M. Descarreaux, P. Mercier, and M. Simoneau, "Sensory reweighting is altered in adolescent patients with scoliosis: Evidence from a neuromechanical model," *Gait Posture*, vol. 42, pp. 558–563, 4 Oct. 2015.

[21] C. Assaiante, S. Mallau, J. L. Jouve, G. Bollini, and M. Vaugoyeau, "Do adolescent idiopathic scoliosis (ais) neglect proprioceptive information in sensory integration of postural control?" *PLoS ONE*, vol. 7, 7 Jul. 2012.

[22] Y. L. Lo *et al.*, "Motor and somatosensory abnormalities are significant etiological factors for adolescent idiopathic scoliosis," *Journal of the Neurological Sciences*, vol. 359, pp. 117–123, 1-2 Dec. 2015.

[23] M. J. Scheyerer *et al.*, "Impact of the vestibular system on the formation and progression to idiopathic scoliosis: A review of literature," *Asian Spine Journal*, vol. 15, pp. 701–707, 5 Oct. 2021.

[24] H.-J. Luo, S.-X. Lin, S.-K. Wu, M.-W. Tsai, and S.-J. Lee, "Comparison of segmental spinal movement control in adolescents with and without idiopathic scoliosis using modified pressure biofeedback unit," *PLOS ONE*, vol. 12, e0181915, 7 Jul. 2017.

[25] N. Antoniadou, V. Hatzitaki, S. Stavridis, and E. Samoladas, "Verticality perception reveals a vestibular deficit in adolescents with idiopathic scoliosis," *Experimental Brain Research*, vol. 236, pp. 1725–1734, 6 Jun. 2018.

[26] H.-R. Weiss, C. Lehnert-Schroth, and M. Moramarco, *Schroth Therapy: Advancements in Conservative Scoliosis Treatment*. LAP LAMBERT Academic Publishing, 2015, pp. 147–225.

[27] R. Gassert and V. Dietz, "Rehabilitation robots for the treatment of sensorimotor deficits: A neurophysiological perspective," *Journal of NeuroEngineering and Rehabilitation*, vol. 15, p. 46, 1 Dec. 2018.

[28] P. K. Jamwal, S. Hussain, and M. H. Ghayesh, "Robotic orthoses for gait rehabilitation: An overview of mechanical design and control strategies," *Proceedings of the Institution of Mechanical Engineers, Part H: Journal of Engineering in Medicine*, vol. 234, pp. 444–457, 5 May 2020.

[29] Q. Miao, M. Zhang, J. Cao, and S. Q. Xie, "Reviewing high-level control techniques on robot-assisted upper-limb rehabilitation," *Advanced Robotics*, vol. 32, pp. 1253–1268, 24 Dec. 2018.

[30] V. Santamaria *et al.*, "Promoting functional and independent sitting in children with cerebral palsy using the robotic trunk support trainer," *IEEE Transactions on Neural Systems and Rehabilitation Engineering*, vol. 28, pp. 2995–3004, 12 Dec. 2020.

[31] A. Eizad, S. Pyo, H. Lee, M. R. Afzal, J. Yoon, and S. K. Lyu, "A 4 dof robot for post-stroke trunk rehabilitation," *International Conference on Control, Automation and Systems*, vol. 2019-October, pp. 514–519, Oct. 2019.

[32] V. Santamaria, T. Luna, M. Khan, and S. Agrawal, "The robotic trunk-support-trainer (trust) to measure and increase postural workspace during sitting in people with spinal cord injury," *Spinal Cord Series and Cases 2020 6:1*, vol. 6, pp. 1–7, 1 Jan. 2020.

[33] *Neuromuscular scoliosis*, 2019.

[34] R. Vialle, C. Thévenin-Lemoine, and P. Mary, "Neuromuscular scoliosis," *Orthopaedics Traumatology: Surgery Research*, vol. 99, S124–S139, 1 Feb. 2013.

[35] M. J. Mulcahey, J. Gaughan, R. Betz, A. Samdani, N. Barakat, and L. Hunter, "Neuromuscular scoliosis in children with spinal cord injury," *Topics in Spinal Cord Injury Rehabilitation*, vol. 19, p. 96, 2 Mar. 2013.

[36] E Forslund *et al.*, "High incidence of falls and fall-related injuries in wheelchair users with spinal cord injury: A prospective study of risk indicators," *Journal of Rehabilitation Medicine*, vol. 49, no. 2, pp. 144–151, Jan. 2017.

[37] E Butler Forslund, K. S. Roaldsen, C Hultling, K Wahman, and E Franzén, "Concerns about falling in wheelchair users with spinal cord injury——validation of the Swedish version of the spinal cord injury falls concern scale," *Spinal Cord*, vol. 54, no. 2, pp. 115–119, Feb. 2016.

[38] M. Persson-Bunke, G. Hägglund, H. Lauge-Pedersen, P. W. MA, and L. Westbom, "Scoliosis in a Total Population of Children With Cerebral Palsy," *Spine*, vol. 37, no. 12, 2012.

[39] N. Sezer, S. Akkuş, and F. G. Uğurlu, "Chronic complications of spinal cord injury.," *World journal of orthopedics*, vol. 6, no. 1, pp. 24–33, Jan. 2015.

[40] T. M. M. F. M. Miller Andrew M.D.; Temple, "Impact of Orthoses on the Rate of Scoliosis Progression in Children with Cerebral Palsy," *Journal of Pediatric Orthopaedics*, vol. 16, no. 3, pp. 332–335, 1996.

[41] S. M. Michael, D Porter, and T. E. Pountney, "Tilted seat position for non-ambulant individuals with neurological and neuromuscular impairment: a systematic review.," *Clinical rehabilitation*, vol. 21, no. 12, pp. 1063–74, Dec. 2007.

[42] T. Ogura, T. Itami, K. Yano, I. Mori, and K. Kameda, "An assistance device to help people with trunk impairment maintain posture," in *2017 International Conference on Rehabilitation Robotics (ICORR)*, IEEE, Jul. 2017, pp. 358–363, ISBN: 978-1-5386-2296-4.

[43] Joon-Hyuk Park, P. Stegall, and S. K. Agrawal, "Dynamic brace for correction of abnormal postures of the human spine," in *2015 IEEE International Conference on Robotics and Automation (ICRA)*, IEEE, May 2015, pp. 5922–5927, ISBN: 978-1-4799-6923-4.

[44] H. Zhang, A. Kadrolkar, and F. C. Sup, "Design and Preliminary Evaluation of a Passive Spine Exoskeleton," *J Med Devices*, vol. 10, no. 1, p. 011 002, Nov. 2015.

[45] J. Park, P. Stegall, and S. K. Agrawal, "Dynamic brace for correction of abnormal postures of the human spine," in *2015 IEEE International Conference on Robotics and Automation (ICRA)*, Seattle, Washington, May 2015, pp. 5922–5927.

[46] M. M. Panjabi, R. A. Brand, and A. A. White, "Three-dimensional flexibility and stiffness properties of the human thoracic spine," *Journal of Biomechanics*, vol. 9, pp. 185–192, 4 Jan. 1, 1976.

[47] M. H. Berkson, A. Nachemson, and A. B. Schultz, "Mechanical properties of human lumbar spine motion segments—-part II: Responses in compression and shear; influence of gross morphology," *Journal of Biomechanical Engineering*, vol. 101, pp. 53–57, 1 Feb. 1, 1979.

[48] A. B. Schultz, D. N. Warwick, M. H. Berkson, and A. L. Nachemson, "Mechanical properties of human lumbar spine motion segments—-part I: Responses in flexion, extension, lateral bending, and torsion," *Journal of Biomechanical Engineering*, vol. 101, pp. 46–52, 1 Feb. 1, 1979.

[49] M. G. Gardner-Morse and I. A. F. Stokes, "Structural behavior of human lumbar spinal motion segments," *Journal of Biomechanics*, Spinal Biomechanics, vol. 37, pp. 205–212, 2 Feb. 1, 2004.

[50] B. D. Stemper, D. Board, N. Yoganandan, and C. E. Wolfla, "Biomechanical properties of human thoracic spine disc segments," *Journal of Craniovertebral Junction and Spine*, vol. 1, p. 18, 1 Jan. 1, 2010.

[51] O. M. O'Reilly, M. F. Metzger, J. M. Buckley, D. A. Moody, and J. C. Lotz, "On the stiffness matrix of the intervertebral joint: Application to total disk replacement," *Journal of Biomechanical Engineering*, vol. 131, pp. 081 007–1 –081007–9, 8 Jul. 2, 2009.

[52] Q. Li, Z. Huang, and J. M. Hervé, "Displacement manifold method for type synthesis of lower-mobility parallel mechanisms," *Science in China Series E: Technological Sciences*, vol. 47, no. 6, pp. 641–650, 2004.

[53] D. Gan, J. S. Dai, J. Dias, R. Umer, and L. Seneviratne, "Singularity-Free Workspace Aimed Optimal Design of a 2T2R Parallel Mechanism for Automated Fiber Placement," *Journal of Mechanisms and Robotics*, vol. 7, no. 4, pp. 41 022–41 029, 2015.

[54] T Ogura, T Itami, K Yano, I Mori, and K Kameda, *An assistance device to help people with trunk impairment maintain posture*, 2017.

[55] Z. Wang, S. Ji, Y. Wan, C. Ou, J. Sun, and G. Wang, "Optimal Design of Parallel Robots for the Prescribed Regular Dexterous Workspace," in *Proceedings of the IEEE International Conference on Automation and Logistics*, IEEE, Aug. 2007, pp. 563–568, ISBN: 978-1-4244-1530-4.

[56] *Genetic algorithm and direct search toolbox user's guide*, The MathWorks, Inc., Natick, MA, USA, 2004.

[57] S. Caro, D. Chablat, P. Wenger, and J. Angeles, "The Isoconditioning Loci of Planar Three-Dof Parallel Manipulators," *Recent Advances in Integrated Design and Manufacturing in Mechanical Engineering*, pp. 129–138, 2003. arXiv: 0708.3896.

[58] F. Ranjbaran, J. Angeles, M. A. González-Palacios, and R. V. Patel, "The mechanical design of a seven-axes manipulator with kinematic isotropy," *Journal of Intelligent & Robotic Systems*, vol. 14, no. 1, pp. 21–41, 1995.

[59] C. C. Nguyen, S. C. Antrazi, Z. L. Zhou, and C. E. Campbell, "Analysis and implementation of a 6 DOF Stewart Platform-based robotic wrist," *Computers and Electrical Engineering*, vol. 17, no. 3, pp. 191–203, 1991.

[60] L.-W. Tsai, *Robot Analysis and Design: The Mechanics of Serial and Parallel Manipulators*, 1st ed. New York, NY, USA: John Wiley & Sons, Inc., 1999, pp. 223–258.

[61] R. Wade, H. Yang, C. McKenna, R. Faria, N. Gummerson, and N. Woolacott, "A systematic review of the clinical effectiveness of eos 2d/3d x-ray imaging system," *European Spine Journal*, vol. 22, pp. 296–304, 2 Feb. 2013.

[62] C. Ophaswongse, R. C. Murray, V. Santamaria, Q. Wang, and S. K. Agrawal, "Human evaluation of wheelchair robot for active postural support (wraps)," *Robotica*, vol. 37, pp. 2132–2146, 12 Dec. 2019.

[63] C. Ophaswongse and S. K. Agrawal, "Optimal design of a novel 3-dof orientational parallel mechanism for pelvic assistance on a wheelchair: An approach based on kinematic geometry and screw theory," *IEEE Robotics and Automation Letters*, vol. 5, pp. 3315–3322, 2 Apr. 2020.

Appendix A: Stiffness Matrix Calculation

First, the stiffness matrix, K, was calculated for each subject at each level, by solving the equation $\mathbf{F} = \mathbf{K}\Delta\mathbf{X}$, where $\Delta\mathbf{X}$ is the displacement vector applied to the subject ($\Delta\mathbf{X} = [\Delta x, \Delta y, \Delta z, \Delta\phi, \Delta\theta, \Delta\psi]^T$) and $\mathbf{F}$ is the vector of forces and moments measured in response ($\mathbf{F} = F_x, F_y, F_z, M_x, M_y, M_z]^T$).

$$\begin{bmatrix} F_x^{(1)} & \dots & F_x^{(n)} \\ \vdots & \ddots & \dots \\ M_z^{(1)} & \dots & M_z^{(n)} \end{bmatrix} = \begin{bmatrix} k_{11} & \dots & k_{16} \\ \vdots & \ddots & \dots \\ k_{61} & \dots & k_{66} \end{bmatrix} \times \begin{bmatrix} \Delta x^{(1)} & \dots & \Delta x^{(n)} \\ \vdots & \ddots & \dots \\ \Delta\psi^{(1)} & \dots & \Delta\psi^{(n)} \end{bmatrix} \tag{A.1}$$

where the superscript (i) denotes the i^{th} force-displacement measurement. The system of equations was solved simultaneously using *linsolve* (MATLAB, MathWorks). The subject's stiffness matrix was then transformed to a dimensionally uniform matrix, and then normalized, before being averaged element-wise over the group.

The dimensions of the stiffness matrix are N/m in the top left quadrant, Nm in the bottom right quadrant, and N in the remaining regions. In order to normalize the matrix, the terms must first be dimension matched. To do this, the force and position vectors ($\mathbf{F}$ and $\mathbf{X}$) are converted to dimensionally uniform vectors ($\tilde{\mathbf{F}}$ and $\tilde{\mathbf{X}}$) by pre-multiplying the conversion matrices ($\mathbf{D_F}$ and $\mathbf{D_X}$):

$$\begin{aligned} \tilde{\mathbf{F}} &= \mathbf{D_F}\mathbf{F} \qquad & \mathbf{D_F} &= \mathrm{diag}(1, 1, 1, L^{-1}, L^{-1}, L^{-1}) \\ & \text{where} & & \\ \tilde{\mathbf{X}} &= \mathbf{D_X}\mathbf{X} & \mathbf{D_X} &= \mathrm{diag}(1, 1, 1, L, L, L) \end{aligned} \tag{A.2}$$

where the characteristic length, L, is the maximum radius of the pelvic ring from its geometric center to the limb attachment points ($0.14m$). Substituting these dimensionally uniform matrices into the equation $\mathbf{F} = \mathbf{K}\Delta\mathbf{X}$, we get $\mathbf{F} = \mathbf{D_F}\mathbf{K}\mathbf{D_X^{-1}}\Delta\tilde{\mathbf{X}}$, and can then obtain the dimensionally uniform matrix, $\tilde{\mathbf{K}}$:

$$\tilde{\mathbf{K}} = \mathbf{D_F}\mathbf{K}\mathbf{D_X^{-1}} \tag{A.3}$$

Each dimensionally uniform stiffness matrix was then normalized to its Frobenius norm, $||\tilde{\mathbf{K}}||_F$, which represents the overall magnitude of the matrix; in other words, the aggregate stiffness. The resulting normalized stiffness matrix, $\hat{\mathbf{K}}$, is as follows:

$$\left\|\tilde{\mathbf{K}}\right\|_F = \sqrt{tr(\tilde{\mathbf{K}}^{\mathbf{T}}\tilde{\mathbf{K}})} = \sqrt{\sum_{i=1}^{6}\sum_{j=1}^{6}\left|\tilde{\mathbf{K}}_{\mathbf{ij}}\right|^2} \tag{A.4}$$

$$\hat{\mathbf{K}} = \tilde{\mathbf{K}}/\left\|\tilde{\mathbf{K}}\right\|_F \tag{A.5}$$

Next, the normalized stiffness matrices are averaged over each group, by taking the mean value of each term, $\hat{\mathbf{K}}_\mathbf{G}$:

$$\hat{\mathbf{K}}_\mathbf{G} = \text{mean}(\hat{\mathbf{K}}_\mathbf{1}, \hat{\mathbf{K}}_\mathbf{2}, \ldots, \hat{\mathbf{K}}_\mathbf{N}) \tag{A.6}$$

where the subscript indicates the subject number.

Finally, we retrieve the scale and units for the group stiffness matrix. We retrieve the scale (de-normalize) by multiplying $\hat{\mathbf{K}}_\mathbf{G}$ by the mean of the Frobenius norms for the subjects in the group, $||\tilde{\mathbf{K}}_\mathbf{G}||$. Then the de-normalized stiffness matrix is de-dimension matched by pre-multiplying by $\mathbf{D_F^{-1}}$ and post multiplying by $\mathbf{D_X}$ to obtain the group average stiffness matrix, $\mathbf{K_G}$:

$$\left\|\tilde{\mathbf{K}}_{\mathbf{G}}\right\|_F = \text{mean}(\left\|\tilde{\mathbf{K}}_{\mathbf{1}}\right\|_F, \left\|\tilde{\mathbf{K}}_{\mathbf{2}}\right\|_F, \ldots, \left\|\tilde{\mathbf{K}}_{\mathbf{N}}\right\|_F) \tag{A.7}$$

$$\mathbf{K}_{\mathbf{G}} = \mathbf{D}_{\mathbf{F}}^{-\mathbf{1}}(\left\|\tilde{\mathbf{K}}_{\mathbf{G}}\right\|_F \cdot \hat{\mathbf{K}}_{\mathbf{G}})\mathbf{D}_{\mathbf{X}} \tag{A.8}$$